

Neoproterozoic tectonothermal evolution of NW India: Evidence from geochemistry and geochronology of granitoids



Jun-Hong Zhao ^{a,*}, Manoj K. Pandit ^b, Wei Wang ^a, Xiao-Ping Xia ^c

^a State Key Laboratory of Geological Processes and Mineral Resources, School of Earth Sciences, China University of Geosciences, Wuhan 430074, China

^b Department of Geology, University of Rajasthan, Jaipur 302004, Rajasthan, India

^c State Key Laboratory of Isotope Geochemistry, Guangzhou Institute of Geochemistry, Chinese Academy of Sciences, Guangzhou 510640, China

ARTICLE INFO

Article history:

Received 12 March 2018

Accepted 20 July 2018

Available online 23 July 2018

Keywords:

Granitoid

Petrogenesis

Neoproterozoic

NW India

Rodinia

ABSTRACT

Neoproterozoic granitoids from the Delhi Fold Belt in NW India record formation and evolution of the marginal orogen in the Rodinia supercontinent. The ca. 976 Ma Moras I-type granites show variable SiO_2 (67.15–75.87 wt %) and CaO (1.10–3.24 wt%) and low REE (59–196 ppm). Their spider diagram is characterized by enrichment of Rb, Th and U and depletion of Na and Ta with positive Pb and negative Sr and Ti anomalies. They have positive ε_{Nd} (_(t)) (+0.41 to +1.40) and ε_{HF} (+2.34 to +9.35) and moderate $\delta^{18}\text{O}$ values (6.48‰ to 7.58‰). These features suggest that the Moras granites were produced by melting of the juvenile mafic crust. However, the ca. 811 Ma Pali and ca. 780 Ma Mirpur A-type granites have high SiO_2 (74.42–78.63 wt%), $\text{K}_2\text{O} + \text{Na}_2\text{O}$ (7.74–8.95 wt%) and REE (266–334 ppm). Their spider diagrams are more enriched in Rb, Th and U and depleted in Ba, Sr and Ti. They have lower ε_{Nd} (−2.28 to +0.84) and ε_{HF} values (−2.31 to +8.62) than, but similar $\delta^{18}\text{O}$ (5.77‰ to 7.01‰) to those of the Moras granites, suggesting that the A-type granites were partial melts of the dehydrated mafic crust in a rift setting. The I- and A-type granites in NW India resulted from physicochemical variations of the lithosphere during evolution of the Rodinia. The Neoproterozoic igneous and sedimentary rocks from the Delhi Fold Belt are well correlated with those from the Jiangnan Fold Belt in South China, suggesting that the two belts probably collected together in the configuration of the Rodinia supercontinent.

© 2018 Elsevier B.V. All rights reserved.

1. Introduction

Granitoids record formation and evolution of the continental crust (Chappell and White 1992; Clemens et al. 2016; Kemp et al. 2007). The processes of their generation and emplacement affect both structures and compositions of the lithosphere (Rudnick and Gao 2003). The petrological variation from I-type to A-type granitoids provides an ideal opportunity to examine the physicochemical natures of the continental crust at different stages of orogenesis (Clemens et al. 1986; Jiang et al. 2009). During the late Mesoproterozoic to Neoproterozoic, many major orogens have formed, including the Delhi Fold Belt in NW India and the Jiangnan Fold Belt in South China in which voluminous granitoids were emplaced. Therefore, correct understanding petrogenesis and tectonic settings of the granitoids are important for clarifying formation and evolution of the continental lithosphere during the assemblage and breakup of the Rodinia supercontinent.

The Great India is suggested to have been collided with the E. Antarctica and Australia during the Neoproterozoic time, and was located at the marginal position of the Rodinia supercontinent (Evans 2009; Li et al. 2008, and references therein). The Delhi Fold Belt is composed mainly of clastic and chemical metasedimentary rocks that were strongly deformed and metamorphosed due to collision between the Marwar and Aravalli Blocks during the early Neoproterozoic, closely correlated to the assemblage of the Rodinia supercontinent (Fig. 1; Vijaya Rao et al. 2000; Bhowmik and Dasgupta 2012). The late Neoproterozoic igneous rocks in the region are suggested to have been contiguous with the Neoproterozoic granitoids from Seychelles and Madagascar, which together formed an active Andean-type arc system in the western margin of the Rodinia (Ashwal et al. 2013; Gregory et al. 2009; Van Lente et al. 2009; Wang et al. 2017a). However, this inferred Andean-type arc system is inconsistent with the synchronous alkaline felsic rocks in the region and the widespread breakup of the Rodinia.

In this paper, we present new elemental and Sr—Nd isotopic data, zircon U—Pb ages and Hf—O isotopic data for the three Neoproterozoic felsic intrusions from NW India. The results show that the early Neoproterozoic I-type granites were derived from a juvenile crust in the arc setting, whereas the late Neoproterozoic A-type granites were partial melts of dehydrated mafic crust in the rift setting.

* Corresponding author at: State Key Laboratory of Geological Processes and Mineral Resources, China University of Geosciences, (Wuhan), China.

E-mail address: jhzha@cug.edu.cn (J.-H. Zhao).

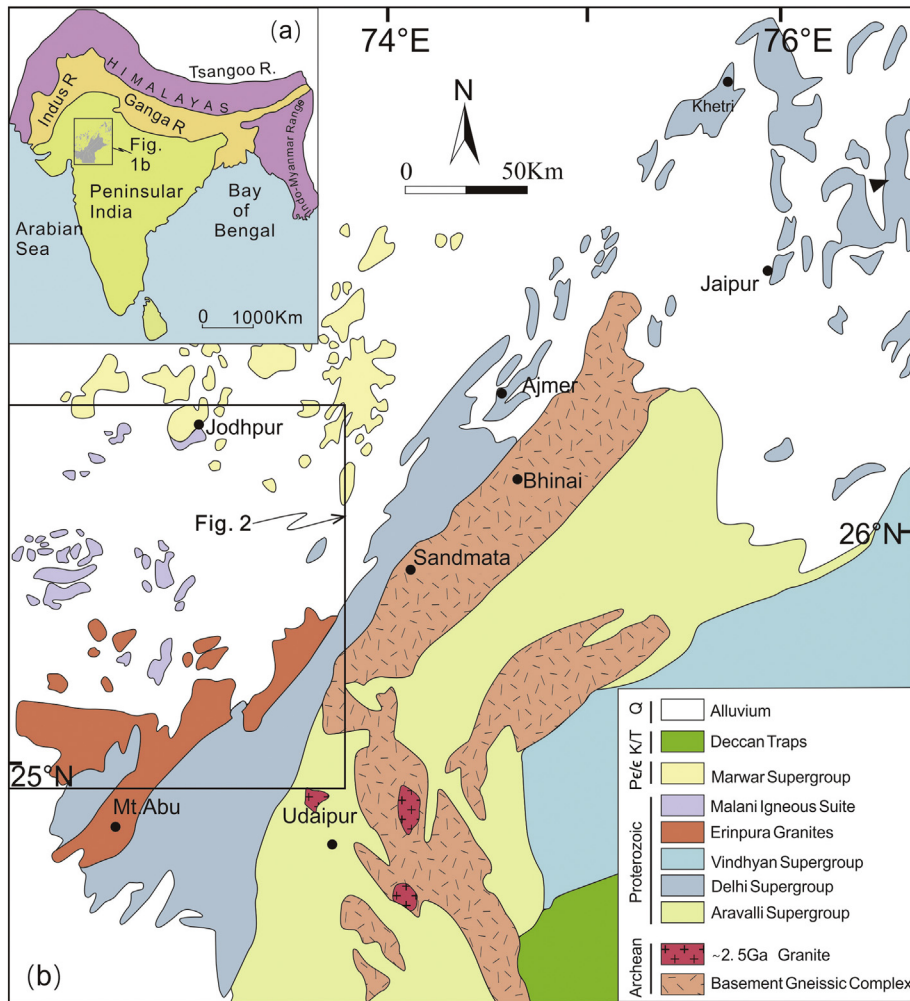


Fig. 1. Simplified geological map showing the distribution of the Precambrian igneous and sedimentary rocks in NW India.

The Neoproterozoic igneous rocks and sedimentary successions in NW India are well correlative with those from the Yangtze Block in South China, suggesting that the two blocks were in the same position in the Rodinia.

2. Geological background

NW Indian (also known as the Aravalli Craton or Aravalli Mountain Region) has a complex Precambrian geological evolutionary history beginning with the 3.3–2.5 Ga TTG basement (Tobisch et al. 1994; Wiedenbeck et al. 1996). The Banded Gneiss Complex (BGC; Heron 1953) also forms basement for two NE-trending Proterozoic (meta)sedimentary sequences, namely the Aravalli and Delhi Supergroups (Fig. 1).

The Aravalli Supergroup consists mainly of metasedimentary and metavolcanic rocks that have a sedimentation time window between 2.2 and 1.6 Ga followed by at least three phases of deformation and greenschist facies metamorphism (McKenzie et al. 2013; Wang et al., 2018a). The Delhi Supergroup covers a much larger area and exposures from Delhi to southwest of Sirohi (Fig. 1). The main lithologies are quartzite, metavolcanics, calc-silicate rocks, schist, conglomerate with subordinate volumes of carbonates that show evidence of polyphase deformation and up to upper amphibolite facies metamorphism (Gupta, 1997). Detrital zircon U–Pb dating underlines a diachronous depositional history for the Delhi Supergroup with a Paleoproterozoic northern domain and a Mesoproterozoic southern domain (McKenzie

et al. 2013; Wang et al. 2017b), named as North and South Delhi Belts, respectively (Sinha-Roy, 1984). The bimodal volcano-sedimentary sequences in two NNE-trending small linear basins, located along the western margin of Delhi Supergroup, were named as Sindreh and Punagarh Groups (Gupta et al. 1980); the recent zircon U–Pb ages and geochemical criteria assign them a much younger status (Dharma Rao et al. 2012; Van Lente et al. 2009; Wang et al. 2017a, 2018b).

Formation of the Delhi Fold Belt is marked by the ~1 Ga collision between the Marwar Block to the west and the Aravalli Block to the east (Vijaya Rao et al. 2000). The suture between the two terranes, also known as the Western Margin Fault, is marked by a linear array of mafic-ultramafic rocks of the Phulad Ophiolite Suite (Tobisch et al. 1994; Volpe and MacDougall 1990). The convergence has resulted in calc-alkaline magmatism within the Sendra – Ambaji belt along western margin of Delhi Fold Belt (Ashwal et al. 2013; Pandit et al. 2003). The 870–820 Ma granite intrusions have been collectively named as Erinpura Granite (Heron 1953; Just et al. 2011; Van Lente et al. 2009), which consist of undeformed granites and variably deformed granite gneisses and form basement of the Sirohi Group (Roy and Jakhar 2002). Both the Erinpura Granite and the Sirohi metasediments underwent deformation with foliations parallel to the regional trend of the Delhi Fold Belt (Just et al. 2011; Pandit et al. 2003). The latest Precambrian event in the region is the most voluminous, predominantly felsic volcanics and intrusive rocks of the Malani Igneous Suite that cover a > 54,000 km² and have zircon U–Pb ages of 770–720 Ma (Fig. 2), further traceable to Nagarparker region in SE Pakistan

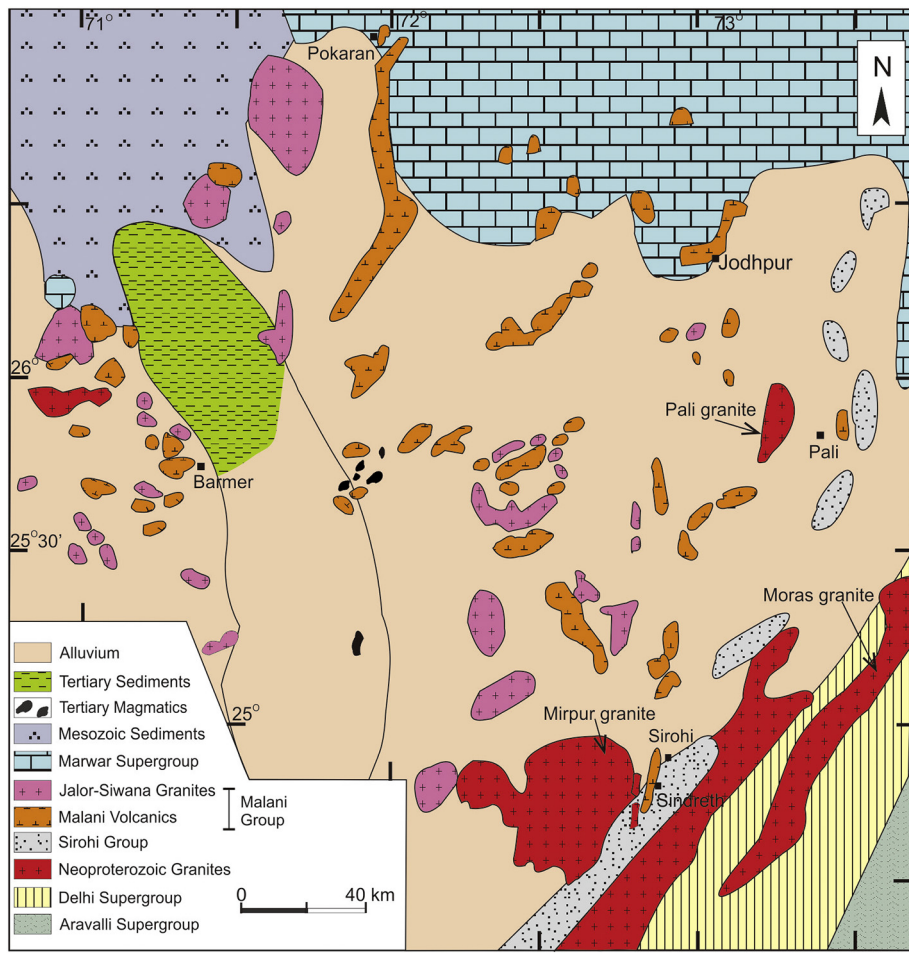


Fig. 2. Geology map of the Neoproterozoic igneous rocks in NW India.

(Bhushan 2000; de Wall et al. 2018; Gregory et al. 2009; Sharma 2005; Wang et al. 2017a).

In this study, three felsic intrusions, including the I-type Moras and the A-type Pali and Mirpur plutons, were collected for integrated petrological, geochronological and geochemical studies (Fig. 2). Rocks from the Moras intrusion consist of fine-grained biotite granite with oriented biotite arrangement (Fig. 3A and B), which may have resulted from later continental collision or ductile shear deformation (Just et al. 2011). They are composed mainly of quartz (35–55%), K-feldspar (15–30%), plagioclase (10–20%), biotite (5–10%) with minor zircon, chlorite and Fe–Ti oxides. Rocks from the Mirpur granite show porphyric texture (Fig. 3C). The phenocryst is K-feldspar (35–40%) that is 5–10 mm long. The matrix is fine-grained and mainly consists of K-feldspar (10–20%), plagioclase (5–15%), quartz (25–30%) and minor biotite. The Pali granites show similar mineral assemblage and texture to those of the Mirpur granites (Fig. 3D). The phenocryst is K-feldspar (40–50%) with length of 5–10 mm. The matrix is fine-grained and dominated by K-feldspar (10–20%), plagioclase (5–15%), quartz (25–35%) and biotite (5%).

3. Analytical methods

3.1. SIMS *in-situ* oxygen isotope analysis

Zircon Cathodoluminescence (CL) images were obtained from the State Key Laboratory of Geological Processes and Mineral Resources (GPMR), China University of Geosciences (CUG), Wuhan. Zircon O isotopes were analyzed using Cameca IMS 1280HR at the State Key Laboratory of Isotope Geochemistry, Guangzhou Institute of Geochemistry,

Chinese Academy of Sciences (CAS). Oxygen isotopes were measured in multi-collector mode using two off-axis Faraday cups. The Nuclear Magnetic Resonance probe was used for magnetic field control with stability better than 2.5 ppm over 16 h on mass 17. One analysis takes ca. 4 min (ca. 2 min pre-sputtering, ca. 1 min automatic beam centering and ca. 40 s integration of oxygen isotopes). The internal precision of single analysis is generally better than $\pm 0.2\%$ for $^{18}\text{O}/^{16}\text{O}$ ratio. The instrumental mass fractionation (IMF) was corrected using standard zircon Penglai that show a recommended ^{18}O values of $5.31 \pm 0.10\%$ with reference to the Vienna standard mean oceanic water (VSMOW) that has a recommended $^{18}\text{O}/^{16}\text{O}$ ratio of 0.0020052 (Li et al. 2010a). The VSMOW-normalized $^{18}\text{O}/^{16}\text{O}$ ratios were corrected for IMF (Li et al. 2010b). Eighteen analyses of standard zircon Penglai yielded ^{18}O value of $5.31 \pm 0.04\%$ ($1\sigma, n = 18$). Analytical procedures and conditions are described in detail by Li et al. (2010a).

3.2. Zircon U–Pb dating and Hf isotope analyses

Zircon U–Pb dating and Lu–Hf isotope analyses were carried out at the GPMR, CUG, Wuhan. Zircon U–Pb dating was performed by an excimer laser ablation system for sampling and an Agilent 7500a ICP-MS for acquiring ion-signal intensities. Each analysis comprises 20–30 s gas blank and 40 s data acquisition. Off-line selection, background integration, analyte signals, time-drift correction and quantitative calibration were performed using software ICPMSDataCal. LA-ICP-MS analytical procedure, common Pb correction and age calculation are described in detail by Liu et al. (2010).

Hf isotopes were analyzed using a Neptune Plus MC-ICP-MS (Thermo Fisher Scientific, Germany) and a Geolas 2005 excimer ArF

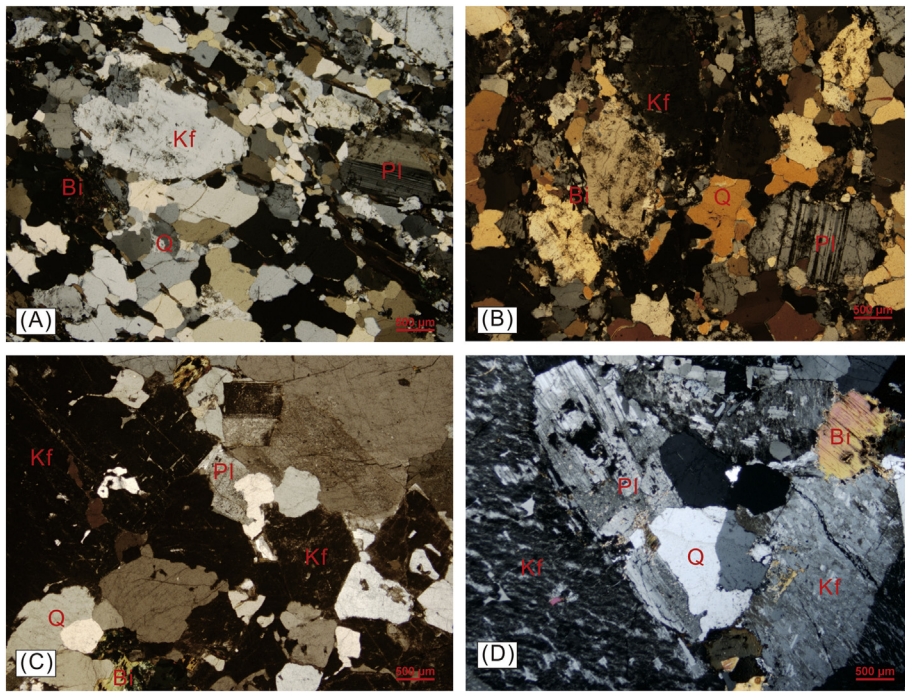


Fig. 3. Photomicrographs showing the mineral assemblages and textures of the Neoproterozoic Moras, Pali and Mirpur granites in NW India. Q = quartz, Kf = K-feldspar, Pl = plagioclase, Bi = biotite.

laser ablation system with a laser spot size of 44 μm (Lambda Physik, Göttingen, Germany). Each measurement comprises 20s background and 50s signal acquisitions. Detailed operating conditions and analytical method are described in Hu et al. (2012). Off-line selection and integration of analyte signals, and mass bias calibrations were performed using ICPMSDataCal (Liu et al. 2010). Zircon, 91500 was served as the external standard. Single-stage model ages (T_{DM}) were calculated relative to the depleted mantle with a present-day ($^{176}\text{Lu}/^{177}\text{Hf}$)_{DM} = 0.0384 and ($^{176}\text{Hf}/^{177}\text{Hf}$)_{DM} = 0.28325, and two-stage model ages (T_{DM}^{C}) were calculated by forcing a growth-curve through the zircon initial ratio with an assumed ($^{176}\text{Lu}/^{177}\text{Hf}$)_C value of 0.015 corresponding to the average continental crust (Griffin et al. 2000).

3.3. Whole-rock geochemical analyses

Major element abundances were obtained using X-ray fluorescence (XRF) on fused glass beads at the GPMR, CUG, Wuhan. Trace elements were analyzed at Institute of Geochemistry, Chinese Academy of Sciences (CAS). The samples were digested by HF + HNO₃ in closed beakers within high-pressure stainless steel bombs. Standard samples, BHVO-1 and SY-4, were used as reference materials and pure elemental standards as external calibration in the experiments. The analytical procedures are described by Qi et al. (2000). The sample solutions were analyzed using an ELAN DRC-e ICP-MS with accuracies better than 5–10%.

3.4. Rb—Sr and Sm—Nd isotopic analyses

The whole rock Sr—Nd isotopic compositions were analyzed in the Radiogenic Isotope Facility at the University of Queensland, Australia. About 100 mg rock powders were dissolved in the mixture of HNO₃ and HF, and dried on a hot plate at 80 °C until fluoride converted to nitrate. The residue was dissolved with 3 ml 2 N HNO₃ and 1.5 ml was loaded onto a stack of Sr-spec, Thru-spec and LN-spec resin columns to separate Sr and Nd from matrix using streamlined procedures. Procedural blanks are ca. 65 and 60 pg for Sr and Nd, respectively. $^{87}\text{Sr}/^{86}\text{Sr}$ and $^{143}\text{Nd}/^{144}\text{Nd}$ measurements were conducted in static mode on a Nu Plasma HR MC-ICP-MS using a modified CETAC ASX-110FR auto-

sampler and a DSN-100 dissolution nebulizing system. The measured $^{87}\text{Sr}/^{86}\text{Sr}$ and $^{143}\text{Nd}/^{144}\text{Nd}$ ratios were corrected for mass fractionation using the exponential law by normalizing to $^{87}\text{Sr}/^{86}\text{Sr} = 0.1194$ and $^{143}\text{Nd}/^{144}\text{Nd} = 0.7219$, respectively. Instrument drift was monitored and calibrated with standards. During our sample analysis, the measured average value for NBS-987 Sr standard is $^{87}\text{Sr}/^{86}\text{Sr} = 0.710250 \pm 0.000006$ ($n = 16, 2\delta$). BCR-2 standard gives $^{87}\text{Sr}/^{86}\text{Sr}$ ratio of 0.705011 ± 0.000005 and $^{143}\text{Nd}/^{144}\text{Nd} = 0.512629 \pm 0.000003$ ($n = 3, 2\delta$), and JG-3 has $^{87}\text{Sr}/^{86}\text{Sr}$ ratios of 0.705387 ± 0.000022 and $^{143}\text{Nd}/^{144}\text{Nd} = 0.512621 \pm 0.000003$ ($n = 3, 2\delta$).

4. Analytical results

4.1. Zircon U—Pb ages and O—Hf isotope compositions

Zircon U—Pb ages, Lu—Hf and O isotopic data are presented in Tables 1 and 2. Initial $^{176}\text{Hf}/^{177}\text{Hf}$ ratios and ε_{Hf} values were calculated using the Lu—Hf isotopic data and the zircon U—Pb ages. CL images of representative zircons are shown in Fig. 4, along with spot locations and the U—Pb ages and oxygen and hafnium isotope results.

4.1.1. The Moras granite

Zircon grains in the Moras granites sample RJ01 are subhedral to euhedral, 100–150 μm in length with aspect ratios of 1:1.5–1:3. In CL images, most grains are dark grey and show magmatic zoning. Some zircons display very complex internal textures, such as inward-penetrating embayment, holes and fractures, faint primary zoning and convolute zoning (Fig. 4), typical features of recrystallization (Pidgeon et al. 1998; Vonlanthen et al. 2012).

Six analyses deviate from the Concordia line. One grain (11) has a $^{206}\text{Pb}/^{238}\text{U}$ age of 1062 ± 9 Ma, probably inherited from country rocks (Table 1). Eleven analyses yield ages ranging from 957 ± 7 Ma to 1002 ± 8 Ma with a weighted mean $^{206}\text{Pb}/^{238}\text{U}$ age of 976 ± 12 Ma (Fig. 5A). The magmatic zircons with concordant ages show large variable initial $^{176}\text{Hf}/^{177}\text{Hf}$ ratios (0.282227 to 0.282438) and ε_{Hf} values (+2.34 to +9.35). Their single- and two-stage Hf model ages range from 1.14 to 1.43 Ga and from 1.23 to 1.70 Ga, respectively. They have

Table 1
Zircon U–Pb ages for the Neoproterozoic granitoids from NW India.

Sample	Pb	Th	U	$^{207}\text{Pb}/^{206}\text{Pb}$	$\pm 1\sigma$	$^{207}\text{Pb}/^{235}\text{U}$	$\pm 1\sigma$	$^{206}\text{Pb}/^{238}\text{U}$	$\pm 1\sigma$	$^{208}\text{Pb}/^{232}\text{Th}$	$\pm 1\sigma$	$^{207}\text{Pb}/^{206}\text{Pb}$	$\pm 1\sigma$	$^{207}\text{Pb}/^{235}\text{U}$	$\pm 1\sigma$	$^{206}\text{Pb}/^{238}\text{U}$	$\pm 1\sigma$	$^{208}\text{Pb}/^{232}\text{Th}$	$\pm 1\sigma$
	U–Pb age (Ma)																		
	(ppm)																		
Sample RJ01 from the Moras intrusion																			
RJ01-1	159	218	151	0.0673	0.0022	1.4745	0.0494	0.1598	0.0014	0.0429	0.0017	848	69	920	20	956	8	850	33
RJ01-2	262	315	425	0.0665	0.0016	1.5583	0.0419	0.1697	0.0017	0.0533	0.0022	833	50	954	17	1011	10	1050	42
RJ01-3	18	19	25	0.0642	0.0072	1.3642	0.1442	0.1608	0.0029	0.0568	0.0028	750	237	874	62	961	16	1117	53
RJ01-4	28	33	53	0.0657	0.0026	1.4278	0.0594	0.1585	0.0020	0.0478	0.0016	798	84	901	25	949	11	943	31
RJ01-5	212	185	692	0.0717	0.0015	1.6507	0.0363	0.1669	0.0019	0.0494	0.0013	976	9	990	14	995	10	974	25
RJ01-6	126	112	472	0.0766	0.0016	1.4372	0.0315	0.1368	0.0018	0.0510	0.0013	1122	10	905	13	827	10	1006	24
RJ01-7	123	116	372	0.0707	0.0014	1.6112	0.0335	0.1646	0.0013	0.0508	0.0012	948	41	975	13	983	7	1001	22
RJ01-8	122	132	320	0.0720	0.0015	1.6571	0.0353	0.1664	0.0015	0.0478	0.0010	987	42	992	14	992	8	944	20
RJ01-9	137	177	174	0.0687	0.0019	1.5183	0.0435	0.1600	0.0015	0.0512	0.0011	889	57	938	18	957	8	1010	22
RJ01-10	226	358	243	0.0811	0.0025	1.6346	0.0478	0.1468	0.0013	0.0431	0.0009	1233	59	984	18	883	8	853	17
RJ01-11	174	163	367	0.0736	0.0014	1.8275	0.0371	0.1792	0.0016	0.0597	0.0013	1031	40	1055	13	1062	9	1173	24
RJ01-12	217	304	178	0.0742	0.0018	1.6838	0.0417	0.1637	0.0016	0.0509	0.0010	1048	49	1002	16	977	9	1003	19
RJ01-13	160	194	293	0.0709	0.0016	1.6535	0.0380	0.1682	0.0015	0.0498	0.0010	954	47	991	15	1002	8	981	19
RJ01-14	290	343	501	0.0727	0.0013	1.6139	0.0289	0.1601	0.0012	0.0513	0.0010	1006	36	976	11	957	7	1011	19
RJ01-15	124	157	162	0.0747	0.0019	1.7269	0.0443	0.1668	0.0015	0.0521	0.0010	1061	50	1019	16	995	8	1027	19
RJ01-16	237	239	498	0.0722	0.0013	1.9162	0.0435	0.1910	0.0027	0.0583	0.0012	992	31	1087	15	1127	14	1145	22
RJ01-17	50	79	150	0.0847	0.0035	1.0775	0.0408	0.0963	0.0027	0.0344	0.0011	1309	80	742	20	593	16	684	22
RJ01-18	111	87	455	0.0742	0.0016	1.6742	0.0363	0.1630	0.0015	0.0493	0.0011	1047	47	999	14	973	8	972	21
Sample RJ81 from the Pali intrusion																			
RJ81-1	111	215	229	0.0899	0.0025	1.7622	0.0483	0.1421	0.0018	0.0361	0.0011	1433	52	1032	18	856	10	717	22
RJ81-2	80	115	185	0.0646	0.0020	1.2046	0.0359	0.1352	0.0012	0.0414	0.0009	761	69	803	17	817	7	820	18
RJ81-3	64	91	140	0.0645	0.0019	1.2287	0.0374	0.1378	0.0015	0.0430	0.0010	761	64	814	17	832	9	850	20
RJ81-4	43	60	97	0.0653	0.0026	1.2282	0.0471	0.1364	0.0014	0.0423	0.0011	785	81	814	21	824	8	836	21
RJ81-5	111	164	237	0.0630	0.0016	1.1614	0.0306	0.1326	0.0011	0.0412	0.0008	709	54	783	14	803	6	815	15
RJ81-6	50	76	66	0.0695	0.0032	1.3295	0.0634	0.1380	0.0018	0.0431	0.0011	922	93	859	28	833	10	852	21
RJ81-7	84	126	180	0.0632	0.0019	1.1728	0.0335	0.1341	0.0011	0.0405	0.0009	717	62	788	16	811	6	802	17
RJ81-8	32	47	53	0.0678	0.0038	1.2414	0.0680	0.1345	0.0018	0.0423	0.0012	861	117	820	31	813	10	838	23
RJ81-9	1575	1635	1886	0.0926	0.0021	1.9828	0.0452	0.1546	0.0015	0.0608	0.0012	1480	44	1110	15	927	8	1193	24
RJ81-10	87	113	122	0.0721	0.0022	1.6109	0.0482	0.1618	0.0014	0.0480	0.0010	987	63	974	19	967	8	947	20
RJ81-11	74	109	151	0.0644	0.0019	1.1841	0.0358	0.1326	0.0012	0.0405	0.0008	754	58	793	17	803	7	802	16
RJ81-12	61	99	121	0.0605	0.0023	1.0960	0.0407	0.1310	0.0014	0.0381	0.0008	620	80	751	20	794	8	756	16
RJ81-13	81	127	129	0.0668	0.0025	1.1876	0.0422	0.1293	0.0012	0.0403	0.0008	831	78	795	20	784	7	799	15
RJ81-14	38	60	78	0.0615	0.0035	1.0776	0.0596	0.1288	0.0016	0.0387	0.0012	654	120	742	29	781	9	768	24
RJ81-15	189	278	350	0.0663	0.0018	1.2671	0.0334	0.1379	0.0011	0.0410	0.0008	817	53	831	15	833	6	813	15
Sample RJ29 from the Mirpur intrusion																			
RJ29-1	204	301	432	0.0777	0.0019	1.3853	0.0362	0.1281	0.0013	0.0428	0.0009	1140	44	883	15	777	8	847	18
RJ29-2	119	171	362	0.0670	0.0015	1.1746	0.0263	0.1263	0.0009	0.0386	0.0008	837	46	789	12	767	5	765	16
RJ29-3	98	142	233	0.0656	0.0017	1.1974	0.0310	0.1320	0.0011	0.0412	0.0008	794	56	799	14	799	6	816	16
RJ29-4	220	290	501	0.0671	0.0013	1.3072	0.0285	0.1400	0.0015	0.0453	0.0009	843	158	849	13	844	8	896	17
RJ29-5	80	123	201	0.0675	0.0018	1.1659	0.0315	0.1248	0.0011	0.0383	0.0008	854	57	785	15	758	6	759	15
RJ29-6	176	219	316	0.0728	0.0023	1.5861	0.0562	0.1569	0.0021	0.0553	0.0016	1009	65	965	22	939	12	1088	31
RJ29-7	183	272	465	0.0680	0.0017	1.1753	0.0281	0.1249	0.0010	0.0398	0.0008	878	52	789	13	759	6	789	16
RJ29-8	216	317	532	0.0663	0.0015	1.1704	0.0270	0.1272	0.0009	0.0404	0.0008	817	49	787	13	772	5	800	16
RJ29-9	122	131	415	0.0664	0.0021	1.3724	0.0448	0.1497	0.0018	0.0487	0.0015	820	65	877	19	900	10	960	29
RJ29-10	169	252	436	0.0662	0.0014	1.1995	0.0261	0.1310	0.0011	0.0395	0.0008	813	46	800	12	794	6	783	16
RJ29-11	202	305	519	0.0634	0.0013	1.1115	0.0221	0.1265	0.0009	0.0389	0.0007	720	44	759	11	768	5	771	13
RJ29-12	217	293	527	0.0683	0.0016	1.3181	0.0297	0.1394	0.0010	0.0426	0.0009	880	48	854	13	842	6	844	16
RJ29-13	147	216	368	0.0634	0.0014	1.1711	0.0269	0.1336	0.0012	0.0402	0.0008	720	48	787	13	808	7	797	15
RJ29-14	271	623	828	0.0699	0.0026	1.1728	0.0457	0.1282	0.0037	0.0252	0.0008	924	71	788	21	778	21	502	16
RJ29-15	372	512	845	0.0657	0.0014	1.3327	0.0295	0.1463	0.0013	0.0422	0.0009	794	44	860	13	880	7	836	17
Sample RJ38 from the Mirpur intrusion																			
RJ38-1	92	128	145	0.0732	0.0031	1.4223	0.0612	0.1419	0.0018	0.0472	0.0014	1020	85	898	26	855	10	932	26
RJ38-2	427	602	769	0.0667	0.0013	1.2701	0.0247	0.1374	0.0011	0.0444									

RJ38-3	545	842	901	0.0769	0.0016	1.3059	0.0290	0.1225	0.0011	0.0394	0.0009	1118	42	848	6	745	18
RJ38-4	1815	3435	2616	0.0669	0.0010	1.0218	0.0164	0.1102	0.0008	0.0354	0.0005	835	161	715	5	674	11
RJ38-5	180	282	487	0.0677	0.0015	1.1094	0.0237	0.1184	0.0009	0.0377	0.0007	859	44	758	11	721	13
RJ38-6	575	624	673	0.0739	0.0021	1.6944	0.0528	0.1643	0.0019	0.0622	0.0017	1039	57	1006	20	981	10
RJ38-7	233	319	567	0.0657	0.0013	1.2652	0.0256	0.1392	0.0012	0.0433	0.0008	794	42	830	12	840	7
RJ38-8	248	322	762	0.0648	0.0013	1.1643	0.0226	0.1297	0.0009	0.0431	0.0008	769	41	784	11	786	5
RJ38-9	212	303	521	0.0652	0.0014	1.1975	0.0255	0.1327	0.0012	0.0425	0.0008	781	41	799	12	803	7
RJ38-10	202	289	589	0.0647	0.0013	1.1747	0.0238	0.1308	0.0010	0.0401	0.0007	765	42	789	11	793	6
RJ38-11	112	166	322	0.0645	0.0015	1.1349	0.0259	0.1271	0.0009	0.0387	0.0007	767	48	770	12	772	5
RJ38-12	217	324	335	0.0709	0.0019	1.3035	0.0369	0.1332	0.0017	0.0444	0.0008	955	56	847	16	806	10
RJ38-13	855	1366	1029	0.0662	0.0012	1.2663	0.0223	0.1378	0.0010	0.0432	0.0007	813	37	831	10	832	6
RJ38-14	711	931	793	0.0856	0.0022	1.7266	0.0469	0.1458	0.0019	0.0500	0.0012	1329	56	1018	17	877	11
RJ38-15	140	228	270	0.0668	0.0016	1.1974	0.0295	0.1293	0.0012	0.0393	0.0008	831	46	799	14	784	7
RJ38-16	114	163	263	0.0697	0.0019	1.3470	0.0363	0.1393	0.0013	0.0414	0.0009	920	54	866	16	841	7

high $\delta^{18}\text{O}$ values (6.48‰ to 7.58‰, Table 2, Fig. 6). The inherited grain (RJ01–11) shows similar ε_{Hf} (+9.84) and $\delta^{18}\text{O}$ values (6.95‰) as compared to the magmatic ones (Fig. 6).

4.1.2. The Pali granite

Zircons in Pali granite sample RJ81 are transparent and colorless, subhedral to euhedral, and range from 50 to 150 μm in length with aspect ratios of 1:1.5 to 1:4 (Fig. 4). They generally display oscillatory zoning and locally unzoned interiors. Some grains have faintly or convolute internal zonings and only few grains preserve core and rim structures (Fig. 4).

Two analyses (1, 9) deviate from the Concordia. One grain (10) shows old concordant $^{206}\text{Pb}/^{238}\text{U}$ age of 967 ± 8 Ma. The remaining analyses yield concordant or nearly concordant $^{206}\text{Pb}/^{238}\text{U}$ ages (781 ± 9 Ma to 833 ± 10 Ma) with a mean $^{206}\text{Pb}/^{238}\text{U}$ age of 811 ± 11 Ma (MSWD = 5.8; Table 1, Fig. 5B). The magmatic zircons show similar ε_{Hf} (+2.52 to +8.62) and relatively lower $\delta^{18}\text{O}$ values (6.15 to 6.82‰), as compared to Moras granite (Fig. 6) except a single magmatic grain (6) with negative ε_{Hf} (−1.08) and higher $\delta^{18}\text{O}$ values (7.8‰) (Table 2). The inherited grain (10) has ε_{Hf} (+7.94) and $\delta^{18}\text{O}$ values (6.52‰) that are in the range of the magmatic zircons (Table 2, Fig. 6).

4.1.3. The Mirpur granite

Two samples (RJ29 and RJ38) from the Mirpur granite body were analyzed for U–Pb ages and Hf–O isotopes (Tables 1 and 2). Zircons from both the samples show close textural similarity and have subhedral to euhedral morphologies, 50 to 300 μm length and aspect ratios of 1:1.5 to 1:3. Majority of grains show oscillatory zoning while some grains are unzoned or show complex convolute interiors (Fig. 4).

Overall 15 points for sample RJ29 were analyzed (Fig. 5C). Four analyses (1, 6, 9 and 15) are clearly discordant, while two grains (4 and 12) show old $^{206}\text{Pb}/^{238}\text{U}$ ages (844 ± 8 and 842 ± 6 Ma), clearly inherited from the Erinpura Granite basement. Nine analyses yield concordant $^{206}\text{Pb}/^{238}\text{U}$ ages ranging from 758 ± 6 Ma to 808 ± 7 Ma, giving a weighted mean $^{206}\text{Pb}/^{238}\text{U}$ age of 775 ± 14 Ma (MSWD = 8.5) that is comparable with the 753 Ma reported in de Wall et al. (2017). Sixteen grains from sample RJ38 were analyzed (Fig. 5D). Eight analyses deviate from the Concordia line. The remaining eight analyses yield two groups of ages, three grains (2, 7, 13) showing old $^{206}\text{Pb}/^{238}\text{U}$ ages (830 ± 6 to 840 ± 7 Ma), and the other five grains with younger $^{206}\text{Pb}/^{238}\text{U}$ ages (772 ± 5 to 803 ± 7 Ma, mean age = 787 ± 14 Ma, MSWD = 3.9).

Most magmatic zircons from the Mirpur granite show $\delta^{18}\text{O}$ values between 5.77 and 7.01‰ and slightly negative to positive ε_{Hf} values (−2.31 to +3.99). Their single- and two-stage Hf model ages range from 1.19 to 1.43 Ga and from 1.45 to 1.83 Ga, respectively. Two magmatic grains show abnormally ε_{Hf} (−1.90 and +14.11) and $\delta^{18}\text{O}$ values (8.40‰ and 7.79‰). Five inherited grains display similar ε_{Hf} (−0.35 to +3.74) and $\delta^{18}\text{O}$ values (5.60 to 6.79‰) to the magmatic zircons (Fig. 6). Their single- and two-stage Hf model ages range from 1.25 to 1.42 and from 1.50 to 1.77 Ga, respectively (Table 2).

4.2. Major and trace elements

The Moras granitoids have variable SiO_2 (67.15–75.87 wt%) and MgO (0.28–1.09 wt%), moderate to high $\text{Na}_2\text{O} + \text{K}_2\text{O}$ (5.46–7.66 wt%) and high $\text{Na}_2\text{O}/\text{K}_2\text{O}$ ratios (0.85–3.17) (Table 3). In addition, they show wide ranges of Fe_2O_3 (1.77–6.50 wt%), CaO (1.10–3.24 wt%), Al_2O_3 (12.81–14.18 wt%) and TiO_2 contents (0.13–0.59 wt%). The rocks have low $\text{Na}_2\text{O} + \text{K}_2\text{O}-\text{CaO}$ and moderate alumina saturation indices ($\text{A/CNK} = 0.96$ –1.04), classifying them as calcic and metaluminous type (Fig. 7). They have a large range of REE abundances (59–196 ppm) and display moderately fractionated LREE patterns ($[\text{La}/\text{Sm}]_n = 1.93$ to 4.07) with variable negative to insignificant positive Eu anomalies ($\text{Eu}/\text{Eu}^* = 0.50$ to 1.08) (Fig. 8). Their primitive mantle-normalized trace-element patterns are characterized by the enrichment of

Table 2Zircon ϵ_{Hf} and $\delta^{18}\text{O}$ values for the Neoproterozoic granites from NW India.

Sample spot	$^{176}\text{Yb}/^{177}\text{Hf}$	1σ	$^{176}\text{Lu}/^{177}\text{Hf}$	1σ	$^{176}\text{Hf}/^{177}\text{Hf}$	1σ	$^{176}\text{Hf}/^{177}\text{Hf}(\text{t})$	ϵ_{Hf}	1σ	T_{DM}	T_{DM}^{C}	$\delta^{18}\text{O}$	$\pm 2\sigma$
Sample RJ01 from the Moras intrusion													
RJ01-1	0.106466	0.001828	0.003745	0.000023	0.282344	0.000027	0.282277	3.60	0.95	1.38	1.60	6.55	0.06
RJ01-4	0.030679	0.000572	0.001213	0.000018	0.282326	0.000019	0.282305	4.44	0.66	1.32	1.54	7.28	0.07
RJ01-5	0.086613	0.002021	0.003459	0.000093	0.282403	0.000019	0.282339	6.67	0.65	1.28	1.44	7.58	0.07
RJ01-7	0.034724	0.000557	0.001503	0.000022	0.282445	0.000018	0.282417	9.19	0.63	1.16	1.26	6.87	0.08
RJ01-8	0.071209	0.003917	0.002688	0.000147	0.282428	0.000032	0.282378	8.02	1.13	1.22	1.35	6.72	0.09
RJ01-9	0.120343	0.004617	0.003460	0.000069	0.282500	0.000019	0.282438	9.35	0.67	1.14	1.23	6.70	0.07
RJ01-11	0.045597	0.001279	0.001613	0.000034	0.282418	0.000019	0.282385	9.84	0.66	1.20	1.28	6.95	0.07
RJ01-12	0.049086	0.003494	0.001488	0.000087	0.282255	0.000022	0.282227	2.34	0.76	1.43	1.70	6.79	0.08
RJ01-13	0.046338	0.001812	0.001572	0.000054	0.282386	0.000019	0.282357	7.48	0.66	1.24	1.39	6.48	0.07
RJ01-14	0.055443	0.002588	0.001595	0.000057	0.282389	0.000020	0.282361	6.61	0.69	1.24	1.41	6.83	0.09
RJ01-15	0.088574	0.002794	0.002523	0.000103	0.282286	0.000024	0.282239	3.12	0.85	1.42	1.66	6.80	0.06
RJ01-18	0.047052	0.001340	0.001416	0.000051	0.282421	0.000017	0.282396	8.21	0.60	1.19	1.32	6.99	0.08
Sample RJ81—from the Pali intrusion													
RJ81-2	0.025195	0.000805	0.000797	0.000028	0.282395	0.000018	0.282383	4.29	0.63	1.21	1.45	6.23	0.06
RJ81-3	0.020342	0.000128	0.000654	0.000002	0.282375	0.000017	0.282365	3.99	0.58	1.23	1.48	6.58	0.06
RJ81-4	0.020111	0.000197	0.000670	0.000009	0.282433	0.000016	0.282422	5.83	0.57	1.15	1.36	6.54	0.09
RJ81-5	0.027205	0.000258	0.000884	0.000009	0.282398	0.000023	0.282385	4.03	0.80	1.20	1.46	6.58	0.08
RJ81-6	0.029257	0.000204	0.0009656	0.000011	0.282237	0.000028	0.282222	-1.08	0.99	1.43	1.81	7.80	0.09
RJ81-7	0.021646	0.000366	0.000698	0.000011	0.282413	0.000019	0.282402	4.83	0.65	1.18	1.41	6.82	0.09
RJ81-8	0.053876	0.000311	0.001803	0.000021	0.282535	0.000027	0.282508	8.62	0.93	1.04	1.17	6.15	0.06
RJ81-10	0.068199	0.001014	0.002545	0.000041	0.282438	0.000041	0.282392	7.94	1.42	1.20	1.33	6.52	0.08
RJ81-11	0.023488	0.000364	0.000772	0.000019	0.282459	0.000018	0.282447	6.24	0.64	1.12	1.31	6.49	0.08
RJ81-12	0.023135	0.000135	0.000770	0.000006	0.282384	0.000026	0.282373	3.38	0.94	1.22	1.49	6.55	0.09
RJ81-13	0.064331	0.001527	0.002108	0.000048	0.282385	0.000028	0.282354	2.52	1.01	1.26	1.54	6.29	0.08
RJ81-14	0.022737	0.000401	0.000752	0.000011	0.282412	0.000021	0.282401	4.10	0.75	1.18	1.43	6.18	0.10
RJ81-15	0.036193	0.000310	0.001123	0.000004	0.282448	0.000019	0.282431	6.32	0.68	1.14	1.33	6.67	0.08
Sample RJ29—from the Mirpur intrusion													
RJ29-2	0.015820	0.000211	0.000548	0.000006	0.282287	0.000023	0.282279	-0.51	0.80	1.35	1.72	6.82	0.11
RJ29-3	0.028403	0.000732	0.000826	0.000018	0.282387	0.000020	0.282375	3.60	0.72	1.22	1.48	6.05	0.10
RJ29-4	0.042927	0.000422	0.001367	0.000011	0.282257	0.000022	0.282235	-0.35	0.78	1.42	1.77	5.60	0.06
RJ29-5	0.018096	0.000075	0.000619	0.000002	0.282400	0.000022	0.282391	3.25	0.75	1.19	1.47	6.20	0.06
RJ29-7	0.021147	0.000268	0.000670	0.000005	0.282382	0.000014	0.282372	2.59	0.49	1.22	1.51	5.77	0.07
RJ29-8	0.023483	0.000211	0.000752	0.000005	0.282294	0.000014	0.282283	-0.25	0.49	1.34	1.70	5.89	0.08
RJ29-10	0.024065	0.000106	0.000750	0.000005	0.282365	0.000020	0.282354	2.73	0.70	1.25	1.53	6.06	0.08
RJ29-11	0.037917	0.001203	0.001130	0.000025	0.282244	0.000069	0.282228	-2.31	2.41	1.43	1.83	6.15	0.09
RJ29-12	0.025311	0.000563	0.000734	0.000010	0.282358	0.000017	0.282347	3.54	0.59	1.25	1.52	6.04	0.09
RJ29-13	0.028140	0.000815	0.000831	0.000019	0.282319	0.000020	0.282307	1.39	0.71	1.31	1.63	6.24	0.08
RJ29-14	0.132035	0.003374	0.003364	0.000058	0.282282	0.000022	0.282233	-1.90	0.77	1.46	1.81	8.40	0.07
Sample RJ38—from the Mirpur intrusion													
RJ38-2	0.054655	0.000617	0.001693	0.000030	0.282305	0.000025	0.282279	0.87	0.89	1.36	1.68	6.03	0.07
RJ14-7	0.023031	0.000406	0.000711	0.000007	0.282364	0.000017	0.282353	3.74	0.59	1.25	1.50	5.71	0.12
RJ14-8	0.024634	0.000184	0.000776	0.000003	0.282306	0.000018	0.282294	0.45	0.62	1.33	1.67	6.76	0.09
RJ38-10	0.020673	0.000785	0.000657	0.000019	0.282400	0.000014	0.282390	3.99	0.49	1.19	1.45	5.93	0.06
RJ38-11	0.021415	0.000647	0.000678	0.000022	0.282320	0.000020	0.282310	0.68	0.71	1.31	1.65	7.01	0.10
RJ38-13	0.045187	0.000947	0.001384	0.000024	0.282324	0.000029	0.282302	1.75	1.02	1.33	1.62	6.79	0.08
RJ38-15	0.033502	0.000902	0.001037	0.000016	0.282330	0.000021	0.282315	1.12	0.73	1.30	1.63	5.95	0.09

LILE (Rb, Ba, Th and U) and depletion of Nb and Ta with positive Pb and negative Sr and Ti anomalies (Fig. 8).

The Pali granites show high SiO₂ (77.03–78.63 wt%) and Na₂O + K₂O (7.74–8.34 wt%), and low MgO (0.14–0.15 wt%), Al₂O₃ (11.41–12.21 wt%) and Fe₂O₃ (0.23–1.02 wt%) abundances. They are calc-alkalic type with uniform A/CNK (1.00–1.04) ratios underline slightly peraluminous affinity (Fig. 7). In the chondrite normalized REE diagrams the samples show LREE fractionation ([La/Sm]_n = 3.64–4.47), almost flat HREE pattern ((Gd/Yb)_n = 0.72–0.94) and strong negative Eu anomalies (Eu/Eu^{*} = 0.05–0.07). The rocks are enriched in Rb, Th and U, and depleted in Nb and Ta and show positive Pb and negative Ti and Sr anomalies (Fig. 8).

The Mirpur granites have relatively higher SiO₂ (74.42–75.35 wt%), Na₂O + K₂O (8.40–8.95 wt%) and moderate MgO (0.33–0.38 wt%), Fe₂O₃ (1.64–2.05 wt%), CaO (0.40–0.74 wt%), Al₂O₃ (12.18–12.54 wt%) and P₂O₅ (0.04–0.06 wt%) contents (Table 3). These rocks classify as alkali-calcic, ferroan and peraluminous type (Fig. 7). Their chondrite normalized REE patterns and trace element characteristics are comparable with the Pali granites (Fig. 8) with overlapping (La/Sm)_n ratios (2.89 to 4.18) but higher (Gd/Yb)_n ratios (1.02 to 1.40). However, the Mirpur

samples show relatively stronger Ta—Nb negative anomalies, higher peaks for Pb and relatively lower abundance levels of compatible elements.

4.3. Rb—Sr and Sm—Nd isotope compositions

Three Moras granite samples were analyzed for whole-rock Sr and Nd isotopes. They have highly variable $^{87}\text{Rb}/^{86}\text{Sr}$ (4.661402–8.882373) and $^{87}\text{Sr}/^{86}\text{Sr}$ ratios (0.771207–0.830663), and yield non-radioactive $^{87}\text{Sr}/^{86}\text{Sr}$ ratios in the range of 0.7019 to 0.7068. Their $^{147}\text{Sm}/^{144}\text{Nd}$ ratios range from 0.1223 to 0.1544 and $^{143}\text{Nd}/^{144}\text{Nd}$ from 0.512233 to 0.512389 with marginally positive ϵ_{Nd} values (+0.42 to +1.40) (Table 4).

Two Pali granite samples show high Rb abundance (574 and 600 ppm) and extremely low Sr concentrations (4.9 and 5.2 ppm) resulting in very high Rb/Sr ratios (439 and 464) and obviously yielding negative initial $^{87}\text{Sr}/^{86}\text{Sr}$ ratios (-1.0395 and -1.1575). Their $^{47}\text{Sm}/^{144}\text{Nd}$ ratios are 0.1421 and 0.1443 and $^{143}\text{Nd}/^{144}\text{Nd}$ are 0.512383 and 0.512391, with slightly positive ϵ_{Nd} values (+0.46 and +0.84; Table 4). Mirpur granites also have high Rb (414 to 498 ppm) and low Sr (28.6 to 68.3



Fig. 4. Cathodoluminescence (CL) images of representative zircons from the Moras (RJ01), Pali (RJ81) and Mirpur granites (RJ29 and RJ38). Figures also show analysis locations, $^{206}\text{Pb}/^{238}\text{U}$ ages, ϵHf and $\delta^{18}\text{O}$ values. Scale bar is 100 μm .

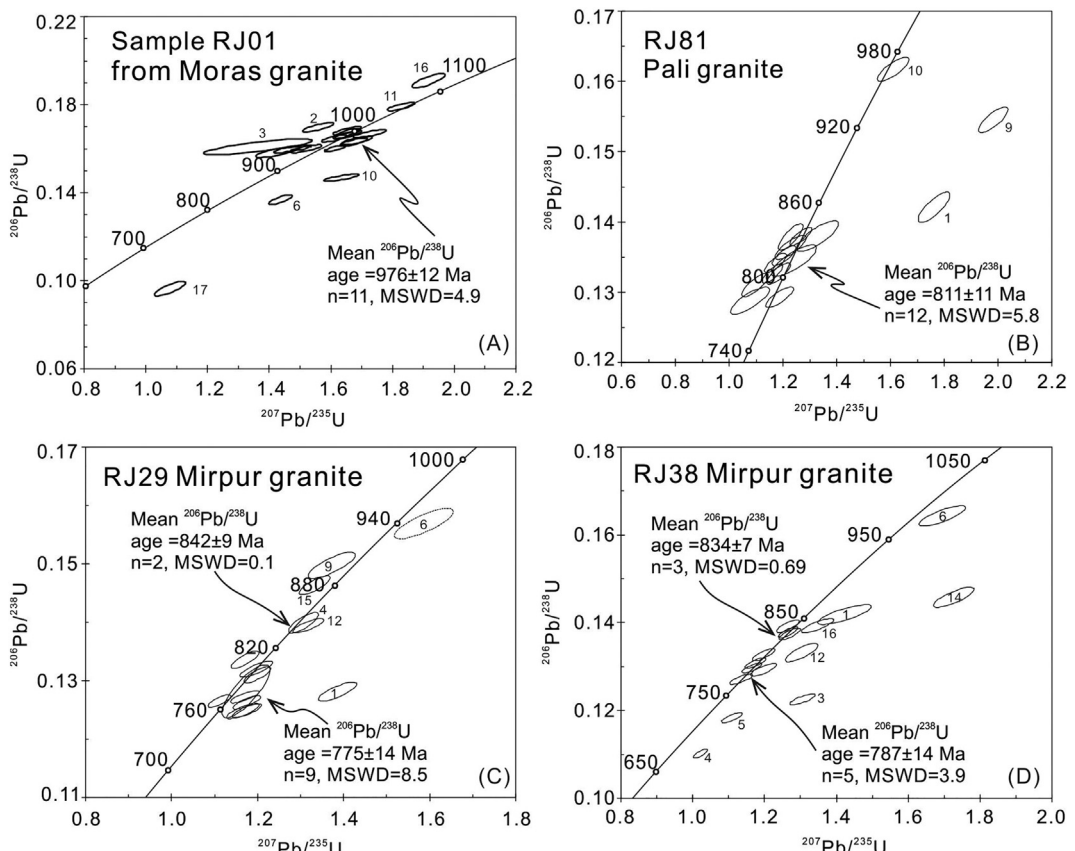


Fig. 5. Zircon U–Pb Concordia diagrams for the granites from Moras, Pali and Mirpur intrusions in NW India.

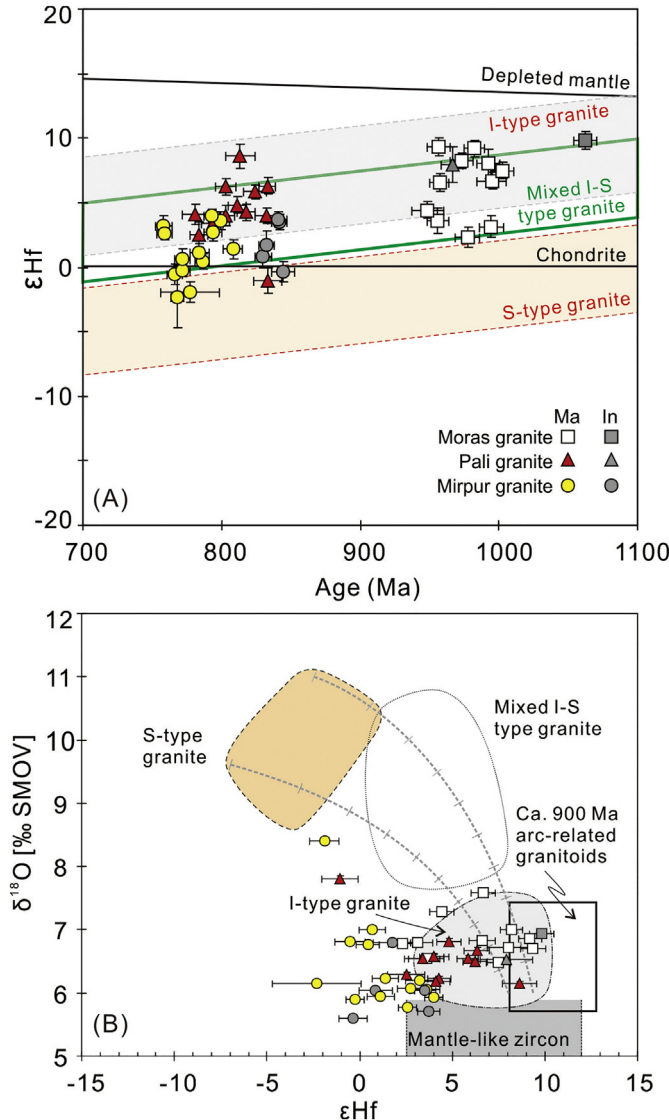


Fig. 6. Plots of ϵ_{Hf} vs. U-Pb age and ϵ_{Hf} for the magmatic (Ma) and inherited (In) zircons with concordant ages from the Moras, Pali and Mirpur granites in NW India. ϵ_{Hf} values are calculated to their individual crystallization ages. Hf evolution lines of chondrite and depleted mantle are from Blichert-Toft and Albarède (1997) and Griffin et al. (2000), respectively. Zircons from the Neoproterozoic I-type, S-type and mixed I-S granitoids in South China are shown for comparison (Zhao et al. 2013).

ppm) and high Rb/Sr ratios (17.85 to 48.59). Although different from Pali samples, these samples also yield very low initial $^{87}\text{Sr}/^{86}\text{Sr}$ ratios (0.5712 to 0.6921). Their $^{47}\text{Sm}/^{144}\text{Nd}$ ratios range from 0.1213 to 0.1287 and $^{143}\text{Nd}/^{144}\text{Nd}$ from 0.512138 to 0.512183 with negative ϵ_{Nd} values of -2.10 to -2.28 that are also distinct from Pali samples (Table 4). High Rb and Rb/Sr and uncommon $^{87}\text{Sr}/^{86}\text{Sr}$ ratios for the Pali and Mirpur granites may have resulted from hydrothermal alteration.

5. Discussion

5.1. Classification of the granitoids

Granitoids are generally subdivide into four types, including I-, S- M- and A-types, which have different lithologies and geochemical compositions (Bonin 2007; Chappell and White 2001). I-type granites are particularly derived from deep crustal igneous materials, whereas S-type granites are partial melts of weathered supracrustal rocks (Chappell and White 2001; Clemens 2003). I-type granites thus

generally have higher CaO and Na₂O and lower K₂O, and display more regular compositional variations than S-type granites (Chappell and White 2001; Clemens 2003). A-type granites normally have higher Na₂O + K₂O, Fe/Mg, Ga/Al and HFSE, and lower CaO, Sr, and Eu than typical I-type varieties (Bonin 2007; King et al. 1997; Whalen et al. 1987), in particular the former is chemically similar to the highly differentiated I-type granites (King et al. 1997; Whalen et al. 1987).

The Moras granites are classified as metaluminous low-K calcic series (Fig. 7). They have low Nb (6.76–14.46 ppm) and Zr + Nb + Ce + Y concentrations (191–528 ppm), moderate FeO*/MgO (3.34–6.06), low $^{104}\text{Ga}/\text{Al}$ (1.91–2.81) and (Na₂O + K₂O)/CaO ratios (1.92–6.93) and thus most samples plot in the field of I-S-M type granitoids (Fig. 9). In addition, the Moras granites have positive ϵ_{Nd} values (+0.42 to +1.40; Table 4). Their magmatic zircons show high ϵ_{Hf} (+2.34 to +9.35) and relatively low $\delta^{18}\text{O}$ values (6.48‰ to 7.58‰). These geochemical features suggest that the Moras granites are I-type granitoids, probably representing southern extension of the Sendra Granites (Pandit et al. 2003).

The Mirpur and Pali granites define distinct geochemical groups as seen in the major element diagrams (Fig. 7). Although geochemically distinct, both the Pali and Mirpur granites are slightly peraluminous and show overall A-type affinity in various discrimination schemes (Fig. 9). They have high Nb (13.5–55.1 ppm) and Zr + Nb + Ce + Y (390–527 ppm), moderate FeO*/MgO (1.50–6.23), high $^{104}\text{Ga}/\text{Al}$ (3.1–4.8) and (Na₂O + K₂O)/CaO ratios (5.09–21.41), and all the samples plot in the field of A-type granitoids (Table 3, Fig. 9).

5.2. Moras I-type granites produced by melting of juvenile mafic crust

I-type granitic melts can be generated by several processes and sources such as melting of igneous (or metagranitic) source in the crust, differentiation of basic magma, or mixing between basaltic and felsic melts thus calling for both mantle- and crustal-inputs in generation of I-type melts (e.g., Chappell and White 2001; Kemp et al. 2007; Zhou et al. 2016).

The potential source for the Moras I-type granites seems to be the Archean basement comprising amphibolites/tonalite - granodioritic rocks in the region (Roy and Jakhar 2002; Wiedenbeck et al. 1996). However, the Moras granites show rather young two-stage Hf model ages (1.23 to 1.70 Ga; Table 2) and Sm—Nd T_{DM} ages (1.53 to 1.96 Ga; Table 4), ruling out the possibility of an Archean source. Alternative source may be the mafic rocks from the overlying Paleo- to Meso-proterozoic Aravalli and Delhi supergroups that occur in close association with pelite - carbonate - quartzite and deep water turbidite facies sediments. It seems quite unlikely that the Moras granites represent selective partial melts of igneous rocks from the Aravalli and Delhi supergroups.

Mafic and ultramafic serpentized rocks (Phulad Ophiolite Suite) are known from the western margin of the Delhi Fold Belt (Volpe and Macdougall, 1990; Khan et al. 2005). Both the Phulad ophiolite and the arc-related igneous rocks suggest that the mantle was modified by the subduction during the early Neoproterozoic (Khan et al. 2005; Pandit et al. 2003). However, mafic and ultramafic rocks of early Neoproterozoic age are rare in the region, as compared to the widespread felsic igneous rocks (Figs. 1 and 2), ruling out the possibility that the Moras I-type granites were produced by differentiation of the mantle derived magmas. The Moras I-type granites show positive ϵ_{Nd} (+0.42 to +1.40; Table 4) and moderate to high zircon ϵ_{Hf} values (+2.34 to +9.35; Table 2) that are closely similar to zircons from the 820-Ma Jiuling granitoids in South China (Fig. 6A), the latter produced by mixing between the supra- and infra-crustal melts (Zhao et al. 2013; Rong et al., 2017). However, the Moras granites show significantly lower $\delta^{18}\text{O}$ values than the mixed I-S type granitoids (Fig. 6B), suggesting that the Moras granites were not formed by mixing between the mantle/infra-crustal and supra-crustal derived melts. Therefore, the Moras I-type granites were more likely to have been produced by

Table 3

Major and trace elements for the Neoproterozoic granitoids from NW Indian.

Moras intrusion											Mirpur intrusion											Pali intrusion						
RJ01	RJ02	RJ03	RJ04	RJ05	RJ06	RJ07	RJ08	RJ09	RJ10	RJ28	RJ29	RJ30	RJ31	RJ32	RJ33	RJ34	RJ35	RJ36	RJ37	RJ38	RJ75	RJ76	RJ77	RJ78	RJ79	RJ80	RJ81	
Major elements (wt%)																												
SiO ₂	71.52	72.28	71.35	67.15	75.87	72.97	72.53	72.09	72.12	71.59	75.35	74.79	74.47	74.55	74.70	75.01	74.65	74.42	75.29	74.42	71.14	78.63	77.72	77.38	77.03	77.19	77.35	77.54
TiO ₂	0.31	0.25	0.39	0.59	0.13	0.25	0.38	0.28	0.33	0.39	0.28	0.27	0.28	0.28	0.29	0.28	0.27	0.26	0.24	0.27	0.60	0.09	0.09	0.09	0.10	0.09	0.09	0.09
Al ₂ O ₃	14.16	13.93	13.71	14.18	12.81	13.55	13.49	14.07	13.38	14.02	12.18	12.54	12.51	12.30	12.41	12.49	12.44	12.49	12.54	12.51	12.79	11.41	12.10	11.78	12.21	11.78	11.70	11.59
Fe ₂ O ₃	3.44	3.09	4.36	6.50	1.77	3.01	3.80	3.32	3.90	3.20	1.81	1.64	1.74	1.85	2.05	1.93	1.75	1.76	1.68	1.70	3.32	0.23	0.35	0.79	0.78	0.88	0.80	1.02
MnO	0.07	0.06	0.08	0.12	0.03	0.07	0.07	0.06	0.07	0.07	0.02	0.02	0.02	0.03	0.03	0.03	0.02	0.02	0.02	0.02	0.05	0.00	0.01	0.02	0.02	0.02	0.01	0.02
MgO	0.53	0.46	0.67	1.09	0.28	0.49	0.66	0.49	0.59	0.86	0.35	0.34	0.34	0.35	0.35	0.33	0.38	0.33	0.35	0.91	0.14	0.15	0.15	0.15	0.14	0.15	0.15	
CaO	2.41	2.21	2.95	3.24	1.10	1.85	2.85	2.31	2.39	2.74	0.41	0.40	0.61	0.74	0.71	0.45	0.50	0.51	0.43	0.62	1.50	0.58	0.59	0.55	0.64	0.58	0.60	0.59
Na ₂ O	4.22	3.98	4.24	3.77	3.51	3.57	4.15	4.15	3.75	4.38	2.40	2.53	2.69	2.81	2.79	2.74	2.80	2.77	2.91	2.80	2.84	3.12	3.17	3.22	3.38	3.19	3.20	3.17
K ₂ O	2.81	3.13	1.40	2.48	4.15	3.59	1.31	2.43	2.66	1.62	6.00	6.10	6.26	5.60	5.72	5.76	5.86	5.73	5.50	5.93	4.82	4.62	4.95	4.78	4.96	5.00	4.84	4.80
P ₂ O ₅	0.08	0.07	0.10	0.16	0.02	0.07	0.09	0.08	0.09	0.11	0.05	0.05	0.05	0.05	0.06	0.05	0.05	0.04	0.05	0.11	0.01	0.01	0.01	0.01	0.01	0.01	0.01	
LOI	0.59	0.46	0.60	0.68	0.39	0.57	0.60	0.52	0.54	0.72	1.04	0.96	0.87	0.96	0.93	0.96	0.74	0.98	0.96	0.95	1.52	0.78	0.82	0.74	0.82	0.73	0.72	0.73
TOL	100.13	99.94	99.85	99.94	100.06	99.98	99.93	99.80	99.82	99.69	99.88	99.63	99.84	99.50	100.02	100.05	99.39	99.37	99.95	99.62	99.60	99.59	99.95	99.53	100.08	99.61	99.47	99.70
Trace elements (ppm)																												
Li	28.8	28.9	33.5	62.0	19.3	29.3	29.1	33.1	33.4	33.5	12.7	9.3	12.0	12.7	15.1	16.2	8.7	12.3	10.5	10.0	27.1	19.2	127	132	143	140	129.1	154
Sc	8.26	8.94	6.94	13.25	4.03	6.99	10.24	6.67	9.32	6.58	5.99	5.68	6.57	7.38	7.18	5.64	6.31	6.22	5.35	6.42	10.79	2.47	2.33	2.84	2.78	2.54	2.28	2.40
Ti	1668	1442	1966	3677	738	1359	2093	1575	1850	2117	1564	1541	1645	1685	1762	1498	1631	1578	1456	1627	3928	492	453	506	507	496	478	534
V	14.3	12.6	17.2	34.5	2.7	11.7	23.4	13.7	17.0	20.8	9.32	9.14	9.42	10.5	9.86	7.70	9.25	9.11	7.87	9.14	37.6	0.97	1.39	1.40	0.76	1.28	1.17	1.29
Cr	5.57	8.72	5.71	6.94	5.78	8.53	7.68	14.31	8.82	11.11	7.58	5.63	6.94	6.55	7.38	7.28	6.69	7.74	6.20	6.41	22.2	7.08	113	4.41	4.58	3.91	7.37	3.98
Mn	546	512	617	1025	286	521	574	508	601	577	185	164	206	252	234	220	177	199	182	199	455	41	82	112	105	155	96	153
Co	4.15	3.75	5.25	9.65	1.33	3.56	5.60	4.17	5.00	5.41	2.03	1.89	2.00	2.12	2.23	2.00	2.11	2.08	1.82	6.96	0.14	1.61	0.20	0.17	0.19	0.22	0.21	
Ni	1.53	2.87	1.91	2.78	1.59	3.28	2.86	6.07	3.32	5.04	1.93	1.48	1.92	1.70	3.13	2.48	2.55	2.47	1.66	1.57	8.00	2.41	80.56	0.56	1.05	1.67	1.34	0.59
Cu	0.58	1.70	2.38	2.25	1.44	1.15	4.18	2.12	1.02	10.6	2.12	2.58	3.99	2.33	2.88	4.32	1.74	2.51	3.66	2.69	23.4	1.58	3.29	1.89	1.69	1.18	1.48	1.44
Zn	49.1	48.9	53.9	92.1	32.6	46.6	55.0	54.1	55.4	47.2	28.7	26.3	31.7	37.7	32.8	37.9	29.3	29.2	25.2	28.7	51.3	37.6	36.2	52.9	47.5	58.4	52.4	65.0
Ga	19.1	18.6	17.2	21.1	13.0	17.0	18.3	18.8	18.0	16.1	20.0	23.4	25.6	28.2	26.7	22.0	24.8	24.9	23.3	26.3	27.8	28.8	28.4	29.4	30.8	28.7	27.6	28.9
Rb	90.1	91.3	67.8	101.4	101.4	117.2	60.4	86.3	108	73.3	518	544	574	565	545	465	566	537	514	560	459	521	633	579	597	592	530	601
Sr	58.6	59.2	72.6	79.9	34.3	49.5	76.6	60.9	65.6	79.3	32.4	33.1	39.7	42.0	34.5	30.1	37.5	33.5	33.2	35.8	73.2	9.8	6.2	6.4	7.3	6.2	6.8	5.7
Y	58.9	52.2	29.7	75.7	15.1	47.1	52.9	35.3	49.9	32.1	54.9	61.5	63.7	74.8	69.5	50.3	65.8	64.3	61.1	69.6	70.4	101	97	105	125	112	110	105
Zr	258	220	269	368	136	213	228	224	288	262	264	267	255	295	300	258	268	260	250	274	284	193	168	192	179	214	174	190
Nb	10.06	9.56	6.76	14.46	6.83	8.35	8.73	9.45	10.5	11.7	14.5	14.7	14.0	16.2	15.8	13.8	14.6	14.2	13.5	14.4	14.7	51.4	52.2	52.6	55.1	48.3	52.0	53.6
Mo	0.37	0.29	0.22	0.29	0.18	0.24	0.25	0.31	0.21	0.34	0.81	0.99	0.81	0.77	0.65	1.29	1.19	0.61	0.49	0.88	1.03	0.53	2.13	0.93	0.80	1.04	0.65	1.83
Cs	6.29	5.93	12.47	8.85	6.22	7.51	5.24	6.23	9.88	6.68	11.9	14.8	15.7	17.2	12.8	14.0	17.3	14.0	11.2	16.1	16.8	12.7	19.9	23.9	24.8	24.9	21.7	26.7
Ba	412	615	211	785	762	538	264	376	673	384	141	143	156	130	133	120	141	136	132	132	158	17.7	17.2	16.6	15.2	17.1	12.1	13.9
La	24.2	27.2	22.9	35.6	16.7	19.5	22.9	24.2	23.0	6.6	26.2	59.5	58.6	67.6	62.8	57.5	57.7	49.8	59.6	61.5	56.1	69.5	59.1	62.8	70.2	65.7	63.3	66.7
Ce	51.7	54.7	46.3	70.6	32.9	48.7	41.9	46.7	46.4	21.1	56.0	123	126	142	134	129	127	115	120	129	122	128	113	106	129	132	127	120
Pr	6.10	6.21	5.20	7.97	3.31	5.09	6.27	5.62	5.11	1.73	6.50	13.80	13.82	15.77	14.97	13.54	13.89	12.28	13.90	14.51	14.04	15.8	13.4	13.9	15.8	14.9	14.2	13.6
Nd	24.1	23.9	19.6	30.8	13.2	19.6	27.3	18.4	20.1	7.63	23.0	51.6	50.6	57.0	54.7	49.6	50.7	44.5	51.1	53.0	52.8	59.4	49.2	49.9	58.2	53.8	52.3	48.3
Sm	6.11	5.81	4.54	7.39	2.65	4.97	7.10	3.86	4.75	2.21	5.85	9.45	9.59	10.70	10.39	8.89	9.50	8.65	9.54	10.11	10.39	12.3	10.4	10.2	12.4	11.3	11.0	9.6
Eu	1.10	1.10	1.19	1.62	0.59	0.88	1.45	1.09	1.25	0.93	0.43	0.59	0.63	0.59	0.58	0.48	0.55	0.53	0.56	0.59	0.87	0.22	0.22	0.24	0.23	0.20	0.21	
Gd	7.28	7.03	4.87	8.75	2.62	5.64	8.39	4.41	5.69	3.15	6.71	9.12	8.99	10.30	9.96	7.6												

Table 3 (continued)

Moras intrusion										Mirpur intrusion										Pali intrusion								
RJ01	RJ02	RJ03	RJ04	RJ05	RJ06	RJ07	RJ08	RJ09	RJ10	RJ28	RJ29	RJ30	RJ31	RJ32	RJ33	RJ34	RJ35	RJ36	RJ37	RJ38	RJ75	RJ76	RJ77	RJ78	RJ79	RJ80	RJ81	
Major elements (wt%)																												
SiO ₂	71.52	72.28	71.35	67.15	75.87	72.97	72.53	72.09	72.12	71.59	75.35	74.79	74.47	74.55	74.70	75.01	74.65	74.42	75.29	74.42	71.14	78.63	77.72	77.38	77.03	77.19	77.35	77.54
TiO ₂	0.31	0.25	0.39	0.59	0.13	0.25	0.38	0.28	0.33	0.39	0.28	0.27	0.28	0.28	0.29	0.28	0.27	0.26	0.24	0.27	0.60	0.09	0.09	0.09	0.10	0.09	0.09	0.09
Al ₂ O ₃	14.16	13.93	13.71	14.18	12.81	13.55	13.49	14.07	13.38	14.02	12.18	12.54	12.51	12.30	12.41	12.49	12.44	12.49	12.54	12.51	12.79	11.41	12.10	11.78	12.21	11.78	11.70	11.59
Fe ₂ O ₃	3.44	3.09	4.36	6.50	1.77	3.01	3.80	3.32	3.90	3.20	1.81	1.64	1.74	1.85	2.05	1.93	1.75	1.76	1.68	1.70	3.32	0.23	0.35	0.79	0.78	0.88	0.80	1.02
MnO	0.07	0.06	0.08	0.12	0.03	0.07	0.07	0.06	0.07	0.07	0.02	0.02	0.02	0.03	0.03	0.03	0.02	0.02	0.02	0.02	0.05	0.00	0.01	0.02	0.02	0.02	0.01	0.02
MgO	0.53	0.46	0.67	1.09	0.28	0.49	0.66	0.49	0.59	0.86	0.35	0.34	0.34	0.35	0.35	0.35	0.33	0.38	0.33	0.35	0.91	0.14	0.15	0.15	0.15	0.14	0.15	0.15
CaO	2.41	2.21	2.95	3.24	1.10	1.85	2.85	2.31	2.39	2.74	0.41	0.40	0.61	0.74	0.71	0.45	0.50	0.51	0.43	0.62	1.50	0.58	0.59	0.55	0.64	0.58	0.60	0.59
Na ₂ O	4.22	3.98	4.24	3.77	3.51	3.57	4.15	4.15	3.75	4.38	2.40	2.53	2.69	2.81	2.79	2.74	2.80	2.77	2.91	2.80	2.84	3.12	3.17	3.22	3.38	3.19	3.20	3.17
K ₂ O	2.81	3.13	1.40	2.48	4.15	3.59	1.31	2.43	2.66	1.62	6.00	6.10	6.26	5.60	5.72	5.76	5.86	5.73	5.50	5.93	4.82	4.62	4.95	4.78	4.96	5.00	4.84	4.80
P ₂ O ₅	0.08	0.07	0.10	0.16	0.02	0.07	0.09	0.08	0.09	0.11	0.05	0.05	0.05	0.05	0.05	0.06	0.05	0.05	0.04	0.05	0.11	0.01	0.01	0.01	0.01	0.01	0.01	0.01
LOI	0.59	0.46	0.60	0.68	0.39	0.57	0.60	0.52	0.54	0.72	1.04	0.96	0.87	0.96	0.93	0.96	0.74	0.98	0.96	0.95	1.52	0.78	0.82	0.74	0.82	0.73	0.72	0.73
TOL	100.13	99.94	99.85	99.94	100.06	99.98	99.93	99.80	99.82	99.69	99.88	99.63	99.84	99.50	100.02	100.05	99.39	99.37	99.95	99.62	99.60	99.59	99.95	99.53	100.08	99.61	99.47	99.70
Trace elements (ppm)																												
Li	28.8	28.9	33.5	62.0	19.3	29.3	29.1	33.1	33.4	33.5	12.7	9.3	12.0	12.7	15.1	16.2	8.7	12.3	10.5	10.0	27.1	19.2	127	132	143	140	129.1	154
Sc	8.26	8.94	6.94	13.25	4.03	6.99	10.24	6.67	9.32	6.58	5.99	5.68	6.57	7.38	7.18	5.64	6.31	6.22	5.35	6.42	10.79	2.47	2.33	2.84	2.78	2.54	2.28	2.40
Ti	1668	1442	1966	3677	738	1359	2093	1575	1850	2117	1564	1541	1645	1685	1762	1498	1631	1578	1456	1627	3928	492	453	506	507	496	478	534
V	14.3	12.6	17.2	34.5	2.7	11.7	23.4	13.7	17.0	20.8	9.32	9.14	9.42	10.5	9.86	7.70	9.25	9.11	7.87	9.14	37.6	0.97	1.39	1.40	0.76	1.28	1.17	1.29
Cr	5.57	8.72	5.71	6.94	5.78	8.53	7.68	14.31	8.82	11.11	7.58	5.63	6.94	6.55	7.38	7.28	6.69	7.74	6.20	6.41	22.2	7.08	113	4.41	4.58	3.91	7.37	3.98
Mn	546	512	617	1025	286	521	574	508	601	577	185	164	206	252	234	220	177	199	182	199	455	41	82	112	105	155	96	153
Co	4.15	3.75	5.25	9.65	1.33	3.56	5.60	4.17	5.00	5.41	2.03	1.89	2.00	2.12	2.23	2.00	2.11	2.08	1.82	1.98	6.96	0.14	1.61	0.20	0.17	0.19	0.22	0.21
Ni	1.53	2.87	1.91	2.78	1.59	3.28	2.86	6.07	3.32	5.04	1.93	1.48	1.92	1.70	3.13	2.48	2.55	2.47	1.66	1.57	8.00	2.41	80.56	0.56	1.05	1.67	1.34	0.59
Cu	0.58	1.70	2.38	2.25	1.44	1.15	4.18	2.12	1.02	10.6	2.12	2.58	3.99	2.33	2.88	4.32	1.74	2.51	3.66	2.69	23.4	1.58	3.29	1.89	1.69	1.18	1.48	1.44
Zn	49.1	48.9	53.9	92.1	32.6	46.6	55.0	54.1	55.4	47.2	28.7	26.3	31.7	37.7	32.8	37.9	29.3	29.2	25.2	28.7	51.3	37.6	36.2	52.9	47.5	58.4	52.4	65.0
Ga	19.1	18.6	17.2	21.1	13.0	17.0	18.3	18.8	18.0	16.1	20.0	23.4	25.6	28.2	26.7	22.0	24.8	24.9	23.3	26.3	27.8	28.8	28.4	29.4	30.8	28.7	27.6	28.9
Rb	90.1	91.3	67.8	101.4	101.4	117.2	60.4	86.3	108	73.3	518	544	574	565	545	465	566	537	514	560	459	521	633	579	579	592	530	601
Sr	58.6	59.2	72.6	79.9	34.3	49.5	76.6	60.9	65.6	79.3	32.4	33.1	39.7	42.0	34.5	30.1	37.5	33.5	33.2	35.8	73.2	9.8	6.2	6.4	7.3	6.2	6.8	5.7
Y	58.9	52.2	29.7	75.7	15.1	47.1	52.9	35.3	49.9	32.1	54.9	61.5	63.7	74.8	69.5	50.3	65.8	64.3	61.1	69.6	70.4	101	97	105	125	112	110	105
Zr	258	220	269	368	136	213	228	224	288	262	264	267	255	295	300	258	268	260	250	274	284	193	168	192	179	214	174	190
Nb	10.06	9.56	6.76	14.46	6.83	8.35	8.73	9.45	10.5	11.7	14.5	14.7	14.0	16.2	15.8	13.8	14.6	14.2	13.5	14.4	14.7	51.4	52.2	52.6	55.1	48.3	52.0	53.6
Mo	0.37	0.29	0.22	0.29	0.18	0.24	0.25	0.31	0.21	0.34	0.81	0.99	0.81	0.77	0.65	1.29	1.19	0.61	0.49	0.88	1.03	0.53	2.13	0.93	0.80	1.04	0.65	1.83
Cs	6.29	5.93	12.47	8.85	6.22	7.51	5.24	6.23	9.88	6.68	11.9	14.8	15.7	17.2	12.8	14.0	17.3	14.0	11.2	16.1	16.8	12.7	19.9	23.9	24.8	24.9	21.7	26.7
Ba	412	615	211	785	762	538	264	376	673	384	141	143	156	130	133	120	141	136	132	132	158	17.7	17.2	16.6	15.2	17.1	12.1	13.9
La	24.2	27.2	22.9	35.6	16.7	19.5	22.9	24.2	23.0	6.6	26.2	59.5	58.6	67.6	62.8	57.5	57.7	49.8	59.6	61.5	56.1	69.5	59.1	62.8	70.2	65.7	63.3	66.7
Ce	51.7	54.7	46.3	70.6	32.9	48.7	41.9	46.7	46.4	21.1	56.0	123	126	142	134	129	127	115	120	129	122	128	113	106	129	132	127	120
Pr	6.10	6.21	5.20	7.97	3.31	5.09	6.27	4.62	5.11	1.73	6.50	13.80	13.82	15.77	14.97	13.54	13.89	12.28	13.90	14.51	14.04	15.8	13.4	13.9	15.8	14.9	14.2	13.6
Nd	24.1	23.9	19.6	30.8	13.2	19.6	27.3	18.4	20.1	7.63	23.0	51.6	50.6	57.0	54.7	49.6	50.7	44.5	51.1	53.0	52.8	59.4	49.2	49.9	58.2	53.8	52.3	48.3
Sm	6.11	5.81	4.54	7.39	2.65	4.97	7.10	3.86	4.75	2.21	5.85	9.45	9.59	10.70	10.39	8.89	9.50	8.65	9.54	10.11	10.39	12.3	10.4	12.4	11.3	11.0	9.6	
Eu	1.10	1.10	1.19	1.62	0.59	0.88	1.45	1.09	1.25	0.93	0.43	0.59	0.63	0.59	0.58	0.48	0.55	0.53	0.56	0.59	0.87	0.22	0.22	0.24	0.23	0.20	0.21	
Gd	7.28	7.03	4.87	8.75	2.62	5.64	8.39	4.41	5.																			

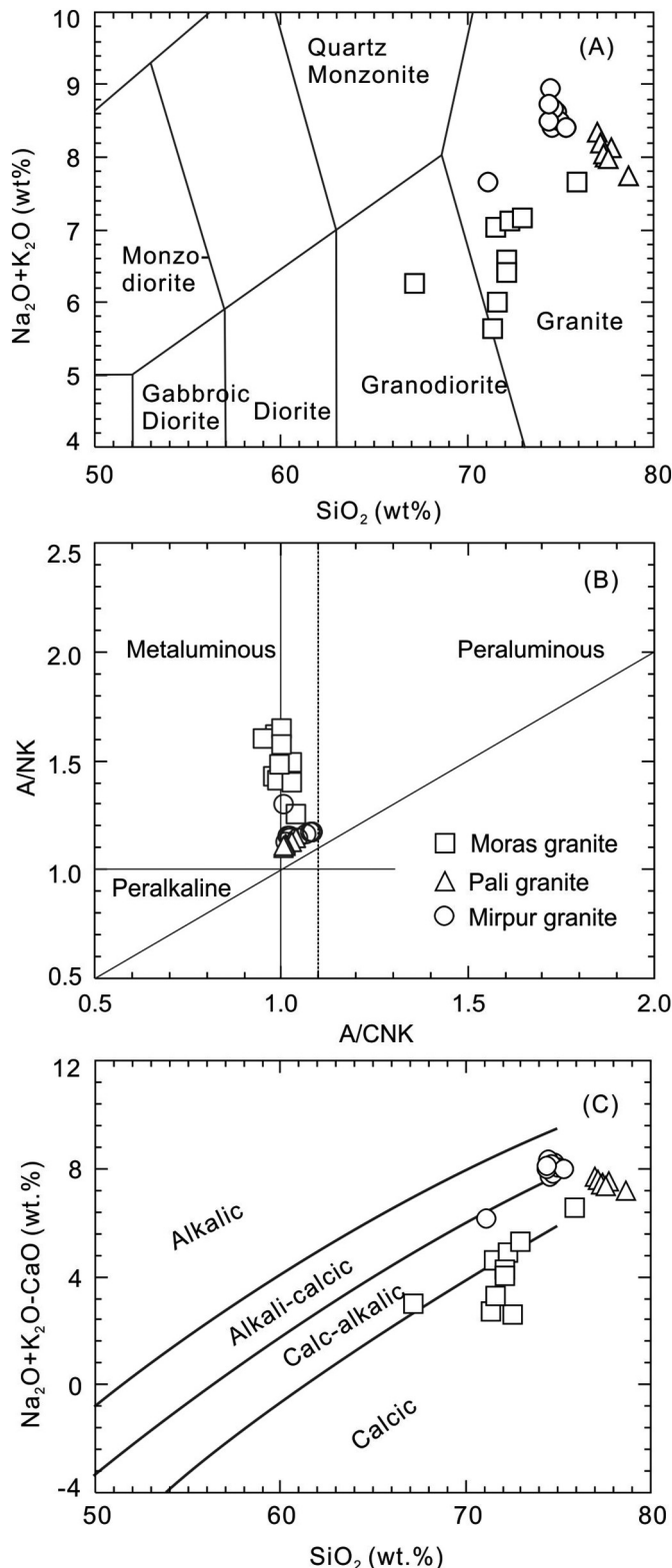


Fig. 7. Plots of Total alkalis vs. SiO_2 (Middlemost 1994), molar $\text{Al}/(\text{Na} + \text{K})$ vs. $\text{Al}/(\text{Ca} + \text{Na} + \text{K})$ (Maniar and Piccoli 1989) and $\text{Na}_2\text{O} + \text{K}_2\text{O}-\text{CaO}$ vs. SiO_2 (Frost et al. 2001) for the granitoids from NW India.

melting of the juvenile mafic crust during the early subduction process. It should be noted that the Moras granites preserve lower whole rock ε_{Nd} and higher zircon $\delta^{18}\text{O}$ values than the mantle source (Fig. 6B), indicating more or less weathering crustal materials involved in their petrogenesis. Their large variable zircon ε_{Hf} values may have been inherited

from a composite source or resulted from crustal contamination during the magma emplacement (e.g. Couzinié et al. 2016; Villaros et al. 2012). Such model is widely used to explain the petrogenesis of I-types in the world.

5.3. Origin of the A-type granitoids

Both the Pali and Mirpur granites show typical lithological and geochemical features of A-type granites that are generally thought to be differentiation products of alkali mantle-derived magmas (Bonin 2007; Clemens et al. 1986; Eby 1992; Whalen et al. 1987) or partial melts of dehydrated crustal rocks (Frost and Frost 2011; King et al. 1997).

5.3.1. No contributions from the mantle source

The original concept of A-type granites suggested that they are formed by fractionation of mantle-derived alkali basalts (Loiselle and Wones 1979). Bonin (2007) further argued that A-type granites are from mantle-derived transitional to alkaline mafic and intermediate magmas. Subsequent studies revealed that some A-type granites were produced by differentiation of mantle-derived melts associated with crustal assimilation during their ascent, producing 'mixed' characteristics (Poitrasson et al. 1995). However, the Neoproterozoic intrusive and extrusive rocks in NW India are mainly of granitic in composition and rare mafic and intermediate rocks have been identified in the region (Bhushan 2000; Gregory et al. 2009). Their zircon $\delta^{18}\text{O}$ values (5.77 ± 0.07 to 8.40 ± 0.07 ; Table 2) are slightly higher than that in equilibrium with mantle sources (5.3 ± 0.6 , Valley et al. 1998). In addition, the Mirpur granites have higher MgO and CaO contents (Table 3), whereas lower ε_{Nd} (-2.10 to -2.28) and ε_{Hf} values (-2.31 to $+3.99$) than the Pali granites ($\varepsilon_{\text{Nd}} = +0.46$ to $+0.84$; $\varepsilon_{\text{Hf}} = +2.52$ to $+8.62$), inconsistent with the crustal contamination trend of the mantle-derived melts. Therefore, the Pali and Mirpur A-type granites in this study were unlikely purely differentiation products of mantle-derived magmas.

5.3.2. Partial melting of dehydrated juvenile mafic rocks

Some workers have suggested that A-type granites are crustal origin. There are many types of crustal rocks that have been proposed for the protolith of A-type granites, such as granulitic metasedimentary (Huang et al. 2011), mafic (Frost and Frost 1997) and felsic metamorphosed igneous rocks (King et al. 1997; Patiño Douce 1997; Zhao et al. 2008). In the study region, possible crustal protolith for the Pali and Mirpur A-type granites include the Archean TTG gneiss, the igneous and sedimentary rocks from the Aravalli and Delhi Supergroups as mentioned above (Fig. 1).

Huang et al. (2011) proposed that the ca. 150 Ma fayalite-bearing A-type granites in South China were produced by high-temperature melting of granulitic metasedimentary rocks. However, the Pali and Mirpur granites show lower zircon $\delta^{18}\text{O}$ (5.77‰ to 8.40‰) and higher ε_{Nd} (-2.31 to $+8.62$) and ε_{Hf} values (-2.28 to $+0.84$) than the A-type granites in South China that have high zircon $\delta^{18}\text{O}$ (8.0‰ to 9.8‰), negative ε_{Hf} (-6.2 to -2.3) and ε_{Nd} (-7.4 to -6.6) (Huang et al. 2011). Their zircon $\delta^{18}\text{O}$ and ε_{Hf} values are also significantly different from those of the Neoproterozoic supracrustal-derived S-type granites in South China (Fig. 6). These isotopic evidences suggest that the A-type granites in this study were not derived from any metasedimentary rocks. Fluid-present melting of tonalitic and granodioritic rocks can also produce oxidizing A-type granites (Frost and Frost 2011; King et al. 1997; Patiño Douce 1997). Although the Archean TTG gneisses are widespread in the region (Fig. 1), the Mirpur and Pali granites show much young Sm—Nd T_{DM} ages (1.62 to 1.73 Ga) and Hf two-stage models ages (1.17 to 1.83 Ga), ruling out the possibility of Archean basement rocks in the source.

Crustal cross-sections and xenoliths indicate that the middle crust is dominated by amphibolite facies to lower granulite facies rocks, while the lower crust mainly comprises mafic granulite facies rocks (Rudnick and Gao 2003). Mafic granulites are generally formed in

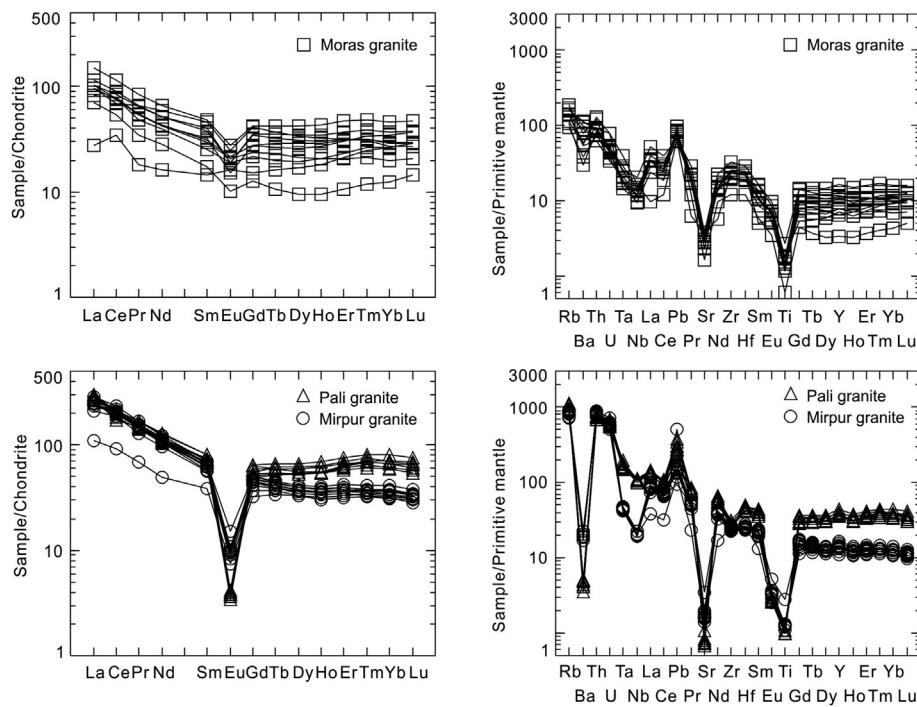


Fig. 8. Chondrite-normalized REE and primitive mantle-normalized trace element patterns for the granitoids from NW India. Normalizing values are from Sun and McDonough (1989).

thickened lower crust by continental collision or mafic magma underplating, and contain appropriate minerals (Opx + Cpx + Plag + Kfs ± Hbl) and chemical compositions required for A-type melts (Landenberger and Collins 1996; Zhao et al. 2008). The Pali and Mirpur A-type granites have higher HFSE and HREE concentrations than the Moras I-type granites, suggesting dry pyroxene-rich sources (Jiang et al. 2005; Landenberger and Collins 1996; Whalen et al. 1987). Their low zircon $\delta^{18}\text{O}$ and high ε_{Hf} values are similar to the juvenile crustal-derived Moras I-type granites and the Neoproterozoic I-type granites in South China (Fig. 6), indicating that the A-type granites in this study were most likely produced by melting of the metamorphosed lower mafic crust. Both their magmatic and inherited zircons defined the same ε_{Hf} evolution arrays (Fig. 6), indicating that the variable Hf isotopes were probably inherited from heterogeneous sources which consisted mainly of mafic rocks with minor felsic or metasedimentary rocks. The Mirpur granites show lower whole rock ε_{Nd} (-2.28 to -2.10) and zircon ε_{Hf} values (-2.31 to $+3.99$) than the Pali granites ($\varepsilon_{\text{Nd}} = 0.46$ to 0.84 ; $\varepsilon_{\text{Hf}} = +2.52$ to $+8.62$), suggesting that more metasedimentary rocks were probably involved (e.g., Huang et al. 2011; Rudnick and Gao 2003). Therefore, the A-type granites in this study may have been derived from the granulitic mafic rocks of the lower crust resulted from underplating of mantle-derived melts.

5.4. Neoproterozoic tectonothermal evolution

The Neoproterozoic magmatism in the NW Indian is characterized by the early Neoproterozoic subduction or collision related igneous rocks (ca. 1.0 Ga), followed by the 870–820 Ma Erinpura Granite and the late Neoproterozoic igneous rocks (<770 Ma) that were generated in extensional setting induced either by slab-retreat (Ashwal et al. 2013; Dharma Rao et al. 2012; Wang et al. 2017a, 2018) or continental rifting (Sharma 2005). Mafic and ultramafic serpentinized bodies in the Phulad Ophiolite Suite of the Kumbalgarh Group (Volpe and Macdougall, 1990) suggest the oceanic slab subduction, basin closure and collision between the Marwar Block and the Aravalli Block. The ca. 1.0 Ga mafic and granitic rocks show arc affinity and that can show continuity into the Moras granite (Ashwal et al. 2013; Pandit et al. 2003; Van Lente et al. 2009). The 976 Ma Moras granite samples in this study plot within the volcanic arc granite (VAG) field in the Nb vs. Y diagram (Fig. 9), indicating that they were probably formed in a marginal continental arc setting (Fig. 10A). The later collision event is recorded by the granulite and amphibolite-facies metamorphism at ca. 0.97–0.93 Ga (Buick et al. 2010). The 870–820 Ma Erinpura granitoids comprise diversity of S-type (mainly) and I-type granitoids that formed in the convergent continental margins between the Marwar Block and the

Table 4
Sr–Nd isotopes for the Neoproterozoic granitoids from NW India.

Sample	Rb (ppm)	Sr (ppm)	$^{87}\text{Rb}/^{86}\text{Sr}$	$^{87}\text{Sr}/^{86}\text{Sr}$	$\pm 2\sigma$	$^{87}\text{Sr}/^{86}\text{Sr}$ i	Sm (ppm)	Nd (ppm)	$^{147}\text{Sm}/^{144}\text{Nd}$	$^{143}\text{Nd}/^{144}\text{Nd}$	$\pm 2\sigma$	$^{143}\text{Nd}/^{144}\text{Nd}_{\text{i}}$	ε_{Nd}	T_{DM} (Ga)
Moras granite														
RJ01	94.3	58.9	4.661	0.771892	0.000009	0.7068	6.31	24.70	0.1544	0.512389	0.000006	0.511400	0.42	1.96
RJ05	99.8	32.9	8.882	0.830663	0.000010	0.7067	2.67	13.20	0.1223	0.512233	0.000006	0.511450	1.40	1.53
RJ09	111	65.1	4.964	0.771207	0.000009	0.7019	4.93	21.00	0.1419	0.512327	0.000006	0.511418	0.77	1.75
Pali granite														
RJ76	600	5.2	439.0	3.927344	0.000025	-1.1575	8.93	37.40	0.1443	0.512383	0.000006	0.511616	0.46	1.69
RJ81	574	4.9	463.9	4.333602	0.000039	-1.0395	10.20	43.40	0.1421	0.512391	0.000006	0.511635	0.84	1.62
Mirpur granite														
RJ29	498	31.8	47.22	1.138315	0.000011	0.6124	9.80	47.10	0.1258	0.512159	0.000007	0.511515	-2.28	1.72
RJ33	462	28.6	48.59	1.112373	0.000011	0.5712	9.09	45.30	0.1213	0.512138	0.000008	0.511518	-2.23	1.67
RJ38	414	68.3	17.85	0.890956	0.000009	0.6921	10.50	49.30	0.1287	0.512183	0.000008	0.511525	-2.10	1.73

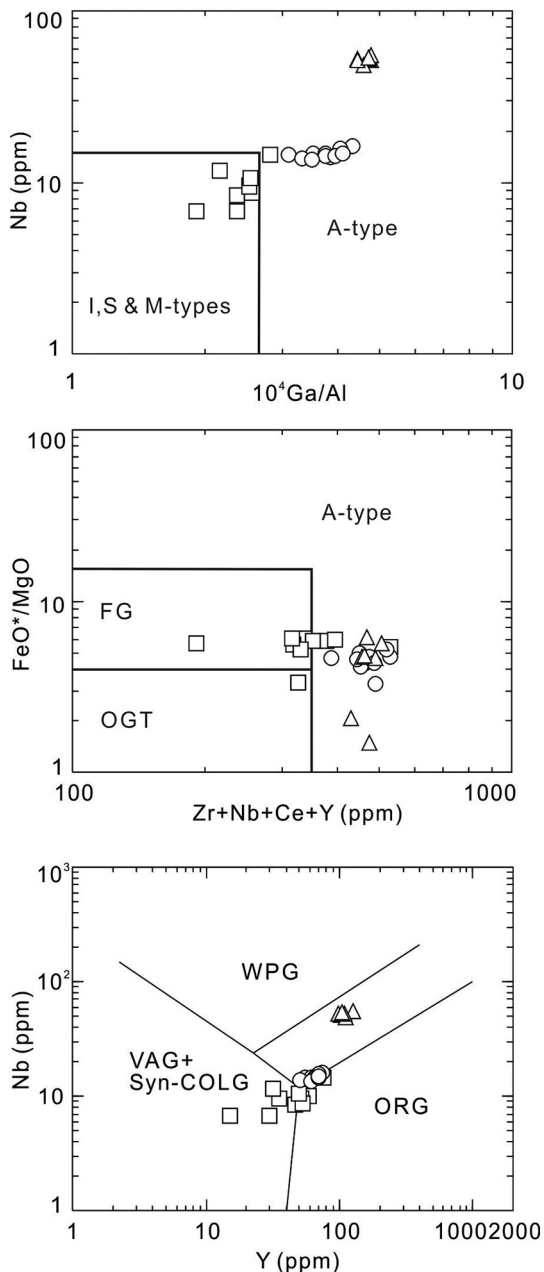


Fig. 9. Plots of Nb vs. 10^4 Ga/Al, FeO^*/MgO vs. $\text{Zr} + \text{Nb} + \text{Ce} + \text{Y}$ and Nb vs. Y for the granitoids from NW India.

Aravalli Block resulted from the Delhi Orogeny (Figs. 1 and 10B; Pradhan et al. 2010).

The ensuing A-type granites represent an independent magmatic event. A-type granites are generally formed in extensional settings (Loiselle and Wones 1979) or post-orogenic and anorogenic settings (Whalen et al. 1987). Eby (1992) classified the A-type granites into the A1-type granites formed in anorogenic settings and A2-type granites emplaced in post-collisional or post-orogenic settings. The Pali and Mirpur A-type granites fall into the WPG (within-plate granite) setting in the Nb vs. Y diagram (Fig. 9). In the plot of Nb-Y-Ce, the A-type granites fall into the A2 group, suggesting a post-orogenic tectonic setting. In the R2-R1 diagram (Batchelor and Bowden 1985), the samples mainly fall in the post-orogenic field. The younger 770–700 Ma Malani Igneous Suite consists of felsic volcanic flows, peralkaline granitoid plutons and mafic dikes (Ashwal et al. 2013; Dharma Rao et al. 2012; Gregory et al. 2009; Van Lente et al. 2009). Therefore, both the A-type granites and the Malani Igneous Suite were probably generated in a

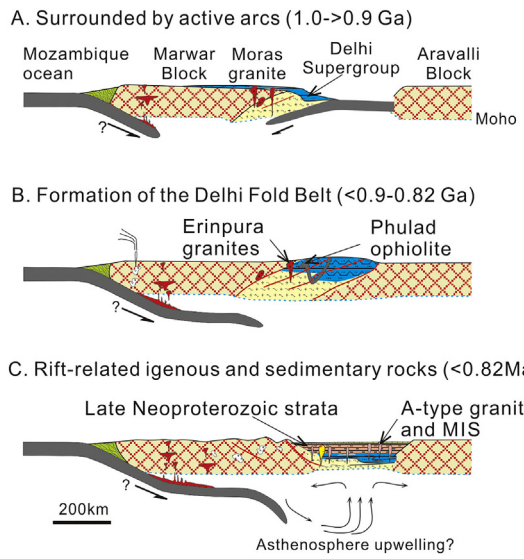


Fig. 10. A sketch diagram showing the secular evolution of NW India during the Neoproterozoic. MIS = Malani Igneous Suite.

rift tectonic setting (Fig. 10C), although they were previously considered to have been formed in an Andean-type magmatic arc (Ashwal et al. 2013; Dharma Rao et al. 2012).

Combined with the geological evidence and the results in this study, we proposed a new tectonic evolution model of the NW India (Fig. 10). During 1.0–0.9 Ga, the oceanic slab was subducted beneath the eastern margin of the Marwar Block (Fig. 10A; Pandit et al. 2003; Ashwal et al. 2013). At around 0.9 Ga, the Marwar and Aravalli Blocks were welded together, leading to the formation of the Delhi Fold Belt. Post-orogenic collapse initiated the generation of 870–820 Ma Erinpura S-type and I-type granitoids (Fig. 10B). After ca. 820 Ma, the asthenospheric upwelling and continental extension, probably resulted from slab bending and rollback beneath the western margin of the Marwar Block, triggered melting of the continental crust to produce voluminous I- and A-type igneous rocks, such as the Pali and Mirpur A-type granites and the Malani Igneous Suite (Fig. 10C). The western margin of the Marwar Block was probably an Andean-type continental margin, similar to the Hannan-Panxi arc system in South China (Zhou et al. 2002).

5.5. Regional correlation

Similar age magmatism and other findings have shown similarity between South China and NW India. South China was assembled by amalgamation of the Yangtze and Cathaysia blocks along the Jiangnan Fold Belt at ca. 830 Ma and then underwent intracontinental extension during the formation of the Nanhua Basin from 820 Ma to 725 Ma (Fig. 11; Zhao et al. 2011; Zheng et al. 2013; Hu et al. 2018). The earliest arc-affinity igneous rocks accompanied the amalgamation between the Yangtze and Cathaysia Blocks are the ~970 Ma Xiwan adakitic rocks and the ~970 Ma Pingshui arc-affinity basaltic rocks (Li and Li 2003). The Jiangnan Fold Belt is mainly composed of the Early Neoproterozoic strata (860–830 Ma Sibao Group and its equivalents) and minor Paleoproterozoic (ca. 1.7 Ga Dahongshan, Dongchuan and Hekou Groups) (Wang and Zhou 2014) and Mesoproterozoic strata (1142 Ma Kunyang Group and 1400–1000 Ma Tianli schist) (Chen et al. 2014; Li et al. 2007). The overlying Late Neoproterozoic strata are best known as the Banxi Group that are mainly composed of pelites, sandstones, conglomerates and minor carbonates deposited in the Nanhua rift basin (Wang and Li 2003). The synchronous igneous rocks are dominated by felsic intrusions; mafic intrusive and extrusive rocks are locally present and show MORB-like geochemical characters.

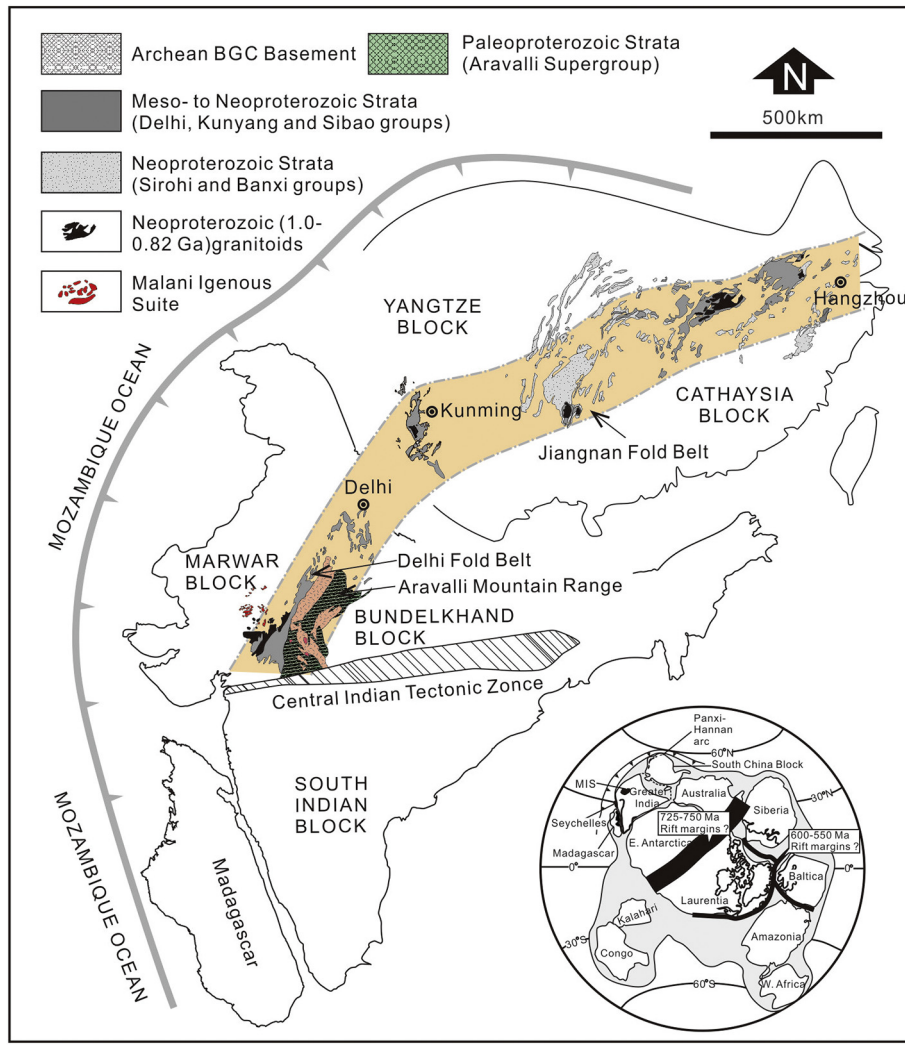


Fig. 11. Possible relationships and palaeogeographic position for India and South China in Rodinia during the Neoproterozoic.

Similarly, both the early Neoproterozoic arc-affinity igneous rocks and sedimentary strata are also found in the eastern margin of the Marwar Block (Pandit et al. 2003). The South Delhi Supergroup comprises the lower Gogunda and upper Kumbalgarh Groups that are dominantly arenaceous and calcareous facies, respectively (Fatima and Khan 2012; Gupta et al. 1980; Wang et al. 2017b). Similarity in lithological characteristics and depositional ages allow a correlation between the South Delhi Supergroup in NW India and the Mesoproterozoic to early Neoproterozoic strata along the southeastern margin of the Yangtze Block in South China (Fig. 11). The Neoproterozoic Sindreh and Punagarh basins in NW India are also chronologically and lithologically similar to the late Neoproterozoic Banxi Group in South China (Wang and Li 2003; Wang and Zhou 2012). In addition, the bimodal extrusive rocks within Sindreh and Punagarh Groups show similarity with rift tectonic affinity of the Banxi Group and its equivalents in South China (Wang and Li 2003).

There are several reconstruction models for the Rodinia based on the limited Neoproterozoic Paleomagnetic data (Evans et al. 2000). India, Madagascar and the Seychelles islands are suggested to have been located along the margins of Rodinia (Ashwal et al. 2013; Cawood et al. 2013; Wang et al. 2017a). Paleomagnetic data for the middle Cambrian sediments and the 820–800 Ma mafic dykes from the western Yangtze Block suggested that South China probably connected with Western Australia and Southern India during the Neoproterozoic time (Niu et al. 2016; Yang et al. 2004). This study further demonstrates that both the sedimentary strata and igneous rocks in NW India and

South China are very similar, suggesting that the two blocks were probably correlated together in the Rodina (Fig. 11).

6. Conclusions

(1) The compositions of the Neoproterozoic granitoids in the Delhi Fold Belt are varied with ages. The early Neoproterozoic Moras I-type granites were produced by melting of the juvenile mafic crust during the assemblage of the Marwar and Aravalli Blocks, whereas the late Neoproterozoic Pali and Mirpur A-type granites were derived from the mafic granulitic rocks of the lower crust.

(2) The Meso- to Neoproterozoic sedimentary successions from the Delhi Fold Belt in NW India are well correlated with those from the Jiangnan Fold Belt in South China. The Neoproterozoic igneous rocks from the two regions are also chronologically and chemically similar. These lines of evidence suggest that the two blocks probably connected together and were located at marginal position of the Rodinia.

Acknowledgments

This work was substantially supported by the National Nature Science Foundation of China (41573020 and 41773027) and the Fundamental Research Funds for the Central Universities, China University of Geosciences (Wuhan). We thank Nelson Eby, Marina V. Luchitskaya and an anonymous referee for their constructive comments that helped to clarify our discussion.

References

- Ashwal, L.D., Solanki, A.M., Pankit, A.K., Corfu, F., Hendriks, B.W.H., Burke, K., Torsvik, T.H., 2013. Geochronology and geochemistry of Neoproterozoic Mt. Abu granitoids, NW India: regional correlation and implications for Rodinia paleogeography. *Precambrian Research* 236, 265–281.
- Batchelor, R.A., Bowden, P., 1985. Petrogenetic interpretation of granitoid rock series using multiactionic parameters. *Chemical Geology* 48, 43–55.
- Bhowmik, S.K., Dasgupta, S., 2012. Tectono-thermal evolution of the banded gneissic complex in Central Rajasthan, NW India: present status and correlation. *Journal of Asia Earth Sciences* 49, 339–348.
- Bhushan, S.K., 2000. Malani rhyolites – a review. *Gondwana Research* 3, 65–77.
- Blichert-Toft, J., Albarède, F., 1997. The Lu-Hf isotope geochemistry of chondrites and the evolution of the mantle-crust system. *Earth and Planetary Science Letters* 148, 243–258.
- Bonin, B., 2007. A-type granites and related rocks: evolution of a concept, problems and prospects. *Lithos* 97, 1–29.
- Buick, I.S., Clark, C., Rubatto, D., Hermann, J., Pandit, M., Hand, M., 2010. Constraints on the Proterozoic evolution of the Aravalli-Delhi Orogenic Belt (NW India) from monazite geochronology and mineral trace element geochemistry. *Lithos* 120, 511–528.
- Cawood, P.A., Wang, Y.J., Xu, Y.J., Zhao, G.C., 2013. Locating South China in Rodinia and Gondwana: a fragment of greater India lithosphere? *Geology* 41, 903–906.
- Chappell, B.W., White, A.J.R., 1992. I-and S-type granites in the Lachlan Fold Belt: transactions of the Royal Society of Edinburgh. *Earth Science* 83, 1–26.
- Chappell, B.W., White, A.J.R., 2001. Two contrasting granite types: 25 years later. *Australian Journal of Earth Sciences* 48, 489–499.
- Chen, W.T., Sun, W.H., Wang, W., Zhao, J.H., Zhou, M.F., 2014. “Grenvillian” intra-plate mafic magmatism in the southwestern Yangtze block, SW China. *Precambrian Research* 242, 138–153.
- Clemens, J.D., 2003. S-type granitic magmas—petrogenetic issues, models and evidence. *Earth-Science Reviews* 61, 1–18.
- Clemens, J.D., Holloway, J.R., White, A.J.R., 1986. Origin of A-type granites: experimental constraints. *American Mineralogist* 71, 317–324.
- Clemens, J.D., Regmi, K., Nicholls, I., Weinberg, R., Maas, R., 2016. The Tynong Pluton, its Mafic Synplutonic Sheets and Igneous Microgranular Enclaves: The Nature of the Mantle Connection in I-Type Granitic Magmas: Contributions to Mineralogy and Petrology 171, 1–17.
- Couzinié, S., Laurent, O., Moyen, J.F., Zeh, A., Bouilhol, P., Villarros, A., 2016. Post-collisional magmatism: crustal growth not identified by zircon Hf-O isotopes. *Earth and Planetary Science Letters* 456, 182–195.
- Dharma Rao, C.V., Santosh, M., Kim, S.W., 2012. Cryogenian volcanic arc in the NW Indian shield: zircon SHRIMP U-Pb geochronology of felsic tuffs and implications for Gondwana assembly. *Gondwana Research* 22, 36–53.
- Eby, G.N., 1992. Chemical subdivision of the A-type granitoids: Petrogenetic and tectonic implications. *Geology* 20, 641–644.
- Evans, D.A.D., 2009. The palaeomagnetically viable, long-lived and all-inclusive Rodinia supercontinent reconstruction. Geological Society, London, Special Publication 327, 371–404.
- Evans, D.A.D., Li, Z.X., Kirschvink, J.L., Wingate, M.T.D., 2000. A high-quality mid-Neoproterozoic paleomagnetic pole from South China, with implications for ice ages and the breakup configuration of Rodinia. *Precambrian Research* 100, 313–334.
- Fatima, S., Khan, M.S., 2012. Petrographic and geochemical characteristics of Mesoproterozoic Kumbalgarh clastic rocks, NW Indian shield: implications for provenance, tectonic setting, and crustal evolution. *International Geology Review* 54, 1113–1144.
- Frost, C.D., Frost, B.R., 1997. Reduced rapakivi-type granites: the tholeiite connection. *Geology* 25, 647–650.
- Frost, C.D., Frost, B.R., 2011. On ferroan (A-type) granitoids: their compositional variability and modes of origin. *Journal of Petrology* 52, 39–53.
- Frost, B.R., Barnes, C.G., Collins, W.J., Arculus, R.J., Ellis, D.J., Frost, C.D., 2001. A geochemical classification for granitic rocks. *Journal of Petrology* 42, 2033–2048.
- Gregory, L.C., Meert, J.G., Bingen, B., Pandit, M.K., Torsvik, T.H., 2009. Paleomagnetism and geochronology of the Malani igneous suite, Northwest India: implications for the configuration of Rodinia and the assembly of Gondwana. *Precambrian Research* 170, 13–26.
- Griffin, W.L., Pearson, N.J., Belousova, E., Jackson, S.E., van Achterbergh, E., O'Reilly, S.Y., Shee, S.R., 2000. The Hf isotope composition of cratonic mantle: LAM-MC-ICPMS analysis of zircon megacrysts in kimberlites. *Geochimica et Cosmochimica Acta* 64, 133–147.
- Gupta, S.N., 1997. The Precambrian Geology of the Aravalli Region, Southern Rajasthan and Northeastern Gujarat. Geological Survey of India, Hyderabad.
- Gupta, S.N., Arora, Y.K., Mathur, R.K., Iqbaluddin, P.B., Sahai, T.N., Sharma, S.B., 1980. Lithostratigraphic Map of the Aravalli Region, Southern Rajasthan and Northeastern Gujarat. Geological Survey of India, Hyderabad.
- Heron, A.M., 1953. Geology of central and southern Rajputana. Geological Survey of India Memoirs 79.
- Hu, Z.C., Liu, Y.S., Gao, S., Liu, W.G., Yang, L., Zhang, W., Tong, X.R., Lin, L., Zong, K.Q., Li, M., Chen, H.H., Zhou, L., 2012. Improved in situ Hf isotope ratio analysis of zircon using newly designed X skimmer cone and jet sample cone in combination with the addition of nitrogen by laser ablation multiple collector ICP-MS. *Journal of Analytical Atomic Spectrometry* 27, 1391–1399.
- Hu, J., Zhang, S., Zhang, G., Tao, S., Zhang, Y., 2018. Geochemistry and tectonic setting of the Eshan granites in the southwestern margin of the Yangtze plate, Yunnan. *Journal of Earth Science* 29, 130–143.
- Huang, H.Q., Li, X.H., Li, W.X., Li, Z.X., 2011. Formation of high $\delta^{18}\text{O}$ fayalite-bearing A-type granite by high temperature melting of granulitic metasedimentary rocks, southern China. *Geology* 39, 903–906.
- Jiang, Y.H., Ling, H.F., Jiang, S.Y., Fan, H.H., Shen, W.Z., Ni, P., 2005. Petrogenesis of a late Jurassic peraluminous volcanic complex and its high-mg, potassic, quenched enclaves at Xiangshan, Southeast China. *Journal of Petrology* 46, 1121–1154.
- Jiang, N., Zhang, S.Q., Zhou, W.G., Liu, Y.S., 2009. Origin of a Mesozoic granite with A-type characteristics from the North China craton: highly fractionated from I-type magmas? *Contributions to Mineralogy and Petrology* 158, 113–130.
- Just, J., Schulz, B., de Wall, H., Jourdan, F., Pandit, M.K., 2011. Monazite CHIME/EPMA dating of Erinpura granitoid deformation: implications for Neoproterozoic tectono-thermal evolution of NW India. *Gondwana Research* 19, 402–412.
- Kemp, A.I.S., Hawkesworth, C.J., Foster, G.L., Paterson, B.A., Woodhead, J.D., Hergt, J.M., Gray, C.M., Whitehouse, M.J., 2007. Magmatic and crustal differentiation history of granitic rocks from Hf-O isotopes in zircon. *Science* 315, 980–983.
- Khan, M.S., Smith, T.E., Raza, M., Huang, J., 2005. Geology, geochemistry and tectonic significance of mafic-ultramafic rocks of Mesoproterozoic Phulad ophiolite suite of South Delhi Fold Belt, NW Indian shield. *Gondwana Research* 8, 553–566.
- King, P.L., White, A.J.R., Chappell, B.W., Allen, C.M., 1997. Characterization and origin of aluminous A-type granites from the Lachlan Fold Belt, southeastern Australia. *Journal of Petrology* 38, 371–391.
- Landenberger, B., Collins, W.J., 1996. Derivation of A-type granites from a dehydrated charnockitic lower crust: evidence from the Chaelundi complex, eastern Australia. *Journal of Petrology* 37, 145–170.
- Li, W.X., Li, X.H., 2003. Adakitic granites within the NE Jiangxi ophiolites, South China: geochemical and Nd isotopic evidence. *Precambrian Research* 122, 29–44.
- Li, Z.X., Warthro, J.A., Occhipinti, S., Zhang, C.L., Li, X.H., Wang, J., Bao, C.M., 2007. Early history of the eastern Sibao Orogen (South China) during the assembly of Rodinia: new mica $^{40}\text{Ar}/^{39}\text{Ar}$ dating and SHRIMP U-Pb detrital zircon provenance constraints. *Precambrian Research* 159, 79–94.
- Li, Z.X., Bogdanova, S.V., Collins, A.S., Davidson, A., De Waele, B., Ernst, R.E., Fitzsimons, I.C., W., Fuck, R.A., Gladkochub, D.P., Jacobs, J., Karlstrom, K.E., Lu, S., Natapov, L.M., Pease, V., Pisarevsky, S.A., Thrane, K., Vernikovsky, V., 2008. Assembly, configuration, and break-up history of Rodinia: a synthesis. *Precambrian Research* 160, 179–210.
- Li, X.H., Li, W.X., Li, Q.L., Wang, X.C., Liu, Y., Yang, Y.H., 2010a. Petrogenesis and tectonic significance of the 850 ma Gangbian alkaline complex in South China: evidence from in situ zircon U-Pb dating, Hf-O isotopes and whole-rock geochemistry. *Lithos* 114, 1–15.
- Li, X.H., Long, W.G., Li, Q.L., Liu, Y., Zheng, Y.F., Yang, Y.H., Chamberlain, K.R., Wan, D.F., Guo, C.H., Wang, X.C., Tao, H., 2010b. Penglai zircon megacrysts: a potential new working reference material for microbeam determination of Hf-O isotopes and U-Pb age. *Geostandards and Geoanalytical Research* 34, 117–134.
- Liu, Y.S., Gao, S., Hu, Z.C., Gao, C.G., Zong, K.Q., Wang, D.B., 2010. Continental and oceanic crust recycling-induced melt-peridotite interactions in the trans-North China Orogen: U-Pb dating, Hf isotopes and trace elements in zircons from mantle xenoliths. *Journal of Petrology* 51, 537–571.
- Loiselle, M.C., Wones, D.R., 1979. Characteristics and origin of anorogenic granites. Geological Society of America, Abstracts with Programs 11, 468.
- Maniar, P.D., Piccoli, P.M., 1989. Tectonic discrimination of granitoids. *Geological Society of America Bulletin* 101, 635–643.
- McKenzie, N.R., Hughes, N.C., Myrow, P.M., Banerjee, D.M., Deb, M., Planavsky, N.J., 2013. New age constraints for the Proterozoic Aravalli-Delhi successions of India and their implications. *Precambrian Research* 238, 120–128.
- Middlemost, E.A., 1994. Naming materials in the magma/igneous rock system. *Earth-Science Reviews* 37, 215–224.
- Niu, J.W., Li, Z.X., Zhu, W.G., 2016. Palaeomagnetism and geochronology of mid-Neoproterozoic Yanbian dykes, South China: implications for a c. 820–800 ma true polar wander event and the reconstruction of Rodinia. Geological Society, London, Special Publication 424, 191–211.
- Pandit, M.K., Carter, L.M., Ashwal, L.D., Tucker, R.D., Torsvik, T.H., Jamtveit, B., Bhushan, S., K., 2003. Age, petrogenesis and significance of 1 Ga granitoids and related rocks from the Senda area, Aravalli craton, NW India. *Journal of Asia Earth Sciences* 22, 363–381.
- Patrón Douce, A.E., 1997. Generation of metaluminous A-type granites by low-pressure melting of calc-alkaline granitoids. *Geology* 25, 743–746.
- Pidgeon, R.T., Nemchin, A.A., Hitchen, G.J., 1998. Internal structures of zircons from Archaean granites from the darling range batholith: implications for zircon stability and the interpretation of zircon U-Pb ages. *Contributions to Mineralogy and Petrology* 132, 288–299.
- Poitrasson, F., Duthou, J.L., Pin, C., 1995. The relationship between petrology and Nd isotopes as evidence for contrasting anorogenic granite genesis: example of the Corsican Province (SE France). *Journal of Petrology* 36, 1251–1274.
- Pradhan, V.R., Meert, J.G., Pandit, M.K., Kamenov, G., Gregory, L.C., Malone, S.J., 2010. India's changing place in global Proterozoic reconstructions: a review of geochronologic constraints and paleomagnetic poles from the Dharwar, Bundelkhand and Marwar cratons. *Journal of Geodynamics* 50, 224–242.
- Qi, L., Hu, J., Goegre, D.C., 2000. Determination of trace elements in granites by inductively coupled plasma - mass spectrometry. *Talanta* 51, 507–513.
- Rong, W., Zhang, S.B., Zheng, Y.F., Gao, P., 2017. Mixing of felsic magmas in granite petrogenesis: geochemical records of zircon and garnet in peraluminous granitoids from South China. *Journal of Geophysical Research Solid Earth* 123, 2738–2769.
- Roy, A.B., Jakhar, S.R., 2002. Geology of Rajasthan: Precambrian to Recent. Scientific Publishers (India), Jodhpur.
- Rudnick, R.L., Gao, S., 2003. Composition of the continental crust, in Rudnick, R.L., Holland, H.D., and Turekian, K.K., eds. *Treatise on Geochemistry*: Amsterdam, Elsevier 3, 1–64.
- Sharma, K.K., 2005. Malani magmatism: an extensional lithospheric tectonic origin. *Geological Society of America Special Papers* 388, 463–476.

- Sinha-Roy, S., 1984. Precambrian crustal interaction in Rajasthan, NW India. *Indian Journal of Earth Sciences* 11, 84–91.
- Sun, S.S., McDonough, W., 1989. Chemical and isotopic systematics of oceanic basalts: implications for mantle composition and processes. Geological Society, London, Special Publication 42, 313–345.
- Tobisch, O.T., Collerson, K.D., Bhattacharyya, T., Mukhopadhyay, D., 1994. Structural relationships and Sr-Nd isotope systematics of polymetamorphic granitic gneisses and granitic-rocks from Central Rajasthan, India – implications for the evolution of the Aravalli craton. *Precambrian Research* 65, 319–339.
- Valley, J.W., Kinny, P.D., Schulze, D.J., Spicuzza, M.J., 1998. Zircon megacrysts from kimberlite: oxygen isotope variability among mantle melts. *Contributions to Mineralogy and Petrology* 133, 1–11.
- Van Lente, B., Ashwal, L.D., Pandit, M.K., Bowring, S.A., Torsvik, T.H., 2009. Neoproterozoic hydrothermally altered basaltic rocks from Rajasthan, Northwest India: implications for late Precambrian tectonic evolution of the Aravalli craton. *Precambrian Research* 170, 202–222.
- Vijaya Rao, V., Rajendra Prasad, B., Reddy, P.R., Tewari, H.C., 2000. Evolution of Proterozoic Aravalli Delhi fold belt in the northwestern Indian shield from seismic studies. *Tectonophysics* 327, 109–130.
- Villalbos, A., Buick, I.S., Stevens, G., 2012. Isotopic variations in S-type granites: an inheritance from a heterogeneous source? *Contributions to Mineralogy and Petrology* 163, 243–257.
- Volpe, A.M., MacDougall, J.D., 1990. Geochemistry and isotopic characteristics of mafic (Phulad ophiolite) and related rocks in the Delhi Supergroup, Rajasthan, India: implications for rifting in the Proterozoic. *Precambrian Research* 48, 167–191.
- Vonlanthen, P., Gerald, J.D.F., Rubatto, D., Hermann, J., 2012. Recrystallization rims in zircon (Valle d'Arbedo, Switzerland): an integrated cathodoluminescence, LA-ICP-MS, SHRIMP, and TEM study. *American Mineralogist* 97, 369–377.
- de Wall, H., Pandit, M.K., Donhauser, I., Schöbel, S., Wang, W., Sharma, K.K., 2018. Evolution and tectonic setting of the Malani – Nagarparkar igneous suite: a Neoproterozoic silicic-dominated large Igneous Province in NW India-SE Pakistan. *Journal of Asian Earth Sciences* 160, 136–158.
- Wang, J., Li, Z.X., 2003. History of Neoproterozoic rift basins in South China: implications for Rodinia break-up. *Precambrian Research* 122, 141–158.
- Wang, W., Zhou, M.F., 2012. Sedimentary records of the Yangtze block (South China) and their correlation with equivalent Neoproterozoic sequences on adjacent continents. *Sedimentary Geology* 265–266, 126–142.
- Wang, W., Zhou, M.F., 2014. Provenance and tectonic setting of the paleo- to Mesoproterozoic Dongchuan group in the southwestern Yangtze block, South China: implication for the breakup of the supercontinent Columbia. *Tectonophysics* 610, 110–127.
- Wang, W., Cawood, P.A., Zhou, M.F., Pandit, M.K., Xia, X.P., Zhao, J.H., 2017a. Low- $\delta^{18}\text{O}$ rhyolites from the Malani igneous suite: a positive test for South China and NW India linkage in Rodinia. *Geophysical Research Letters* 44, 10298–10305.
- Wang, W., Cawood, P.A., Zhou, M.F., Pandit, M.K., Chen, W.T., 2017b. Zircon U-Pb age and Hf isotope evidence for Eoarchean crustal remnant, and crustal growth and reworking respond to supercontinental cycles in NW India. *Journal of the Geological Society* 174, 759–772.
- Wang, W., Cawood, P.A., Pandit, M.K., Zhou, M.F., Zhao, J.H., 2018a. Evolving passive- and active-margin tectonics of the Paleoproterozoic Aravalli Basin, NW India. *Geological Society of American Bulletin* <https://doi.org/10.1130/B35027.1>.
- Wang, W., Pandit, M.K., Zhao, J.-H., Chen, W.-T., Zheng, J.-P., 2018b. Slab break-off triggered lithosphere – asthenosphere interaction at a convergent margin: the Neoproterozoic bimodal magmatism in NW India. *Lithos* 296–299, 281–296.
- Whalen, J.B., Currie, K.L., Chappell, B.W., 1987. A-type granites: geochemical characteristics, discrimination and petrogenesis. *Contributions to Mineralogy and Petrology* 95, 407–419.
- Wiedenbeck, M., Goswami, J.N., Roy, A.B., 1996. Stabilization of the Aravalli craton of northwestern India at 2.5 Ga: an ion microprobe zircon study. *Chemical Geology* 129, 325–340.
- Yang, Z.Y., Sun, Z.M., Yang, T.S., Pei, J.L., 2004. A Long Connection (750–380 Ma) between South China and Australia: Paleomagnetic Constraints: *Earth and Planetary Science Letters* 220, 423–434.
- Zhao, X.F., Zhou, M.F., Li, J.W., Wu, F.Y., 2008. Association of Neoproterozoic A- and I-type granites in South China: implications for generation of A-type granites in a subduction-related environment. *Chemical Geology* 257, 1–15.
- Zhao, J.H., Zhou, M.F., Yan, D.P., Zheng, J.P., Li, J.W., 2011. Reappraisal of the ages of Neoproterozoic strata in South China: no connection with the Grenvillian orogeny. *Geology* 39, 299–302.
- Zhao, J.H., Zhou, M.F., Zheng, J.P., 2013. Constraints from zircon U-Pb ages, O and Hf isotopic compositions on the origin of Neoproterozoic peraluminous granitoids from the Jiangnan Fold Belt, South China. *Contributions to Mineralogy and Petrology* 166, 1505–1519.
- Zheng, Y.F., Xiao, W.J., Zhao, G.C., 2013. Introduction to tectonics of China. *Gondwana Research* 23, 1189–1206.
- Zhou, M.F., Yan, D.P., Kennedy, A.K., Li, Y.Q., Ding, J., 2002. SHRIMP zircon geochronological and geochemical evidence for Neoproterozoic arc-related magmatism along the western margin of the Yangtze block, South China. *Earth and Planetary Science Letters* 196, 51–67.
- Zhou, Z., Ma, C., Xie, C., Wang, L., Liu, Y., Liu, W., 2016. Genesis of highly fractionated I-type granites from Fengshun complex: implications to tectonic evolutions of South China. *Journal of Earth Science* 27, 444–460.